LIÈGE université Library

https://lib.uliege.be

https://matheo.uliege.be

Mémoire

Auteur : Higgins, Owen
Promoteur(s) : 8568; Grodent, Denis
Faculté : Faculté des Sciences
Diplôme : Master en sciences spatiales, à finalité approfondie
Année académique : 2020-2021
URI/URL : http://hdl.handle.net/2268.2/12691

Avertissement à l'attention des usagers :

Tous les documents placés en accès ouvert sur le site le site MatheO sont protégés par le droit d'auteur. Conformément aux principes énoncés par la "Budapest Open Access Initiative"(BOAI, 2002), l'utilisateur du site peut lire, télécharger, copier, transmettre, imprimer, chercher ou faire un lien vers le texte intégral de ces documents, les disséquer pour les indexer, s'en servir de données pour un logiciel, ou s'en servir à toute autre fin légale (ou prévue par la réglementation relative au droit d'auteur). Toute utilisation du document à des fins commerciales est strictement interdite.

Par ailleurs, l'utilisateur s'engage à respecter les droits moraux de l'auteur, principalement le droit à l'intégrité de l'oeuvre et le droit de paternité et ce dans toute utilisation que l'utilisateur entreprend. Ainsi, à titre d'exemple, lorsqu'il reproduira un document par extrait ou dans son intégralité, l'utilisateur citera de manière complète les sources telles que mentionnées ci-dessus. Toute utilisation non explicitement autorisée ci-avant (telle que par exemple, la modification du document ou son résumé) nécessite l'autorisation préalable et expresse des auteurs ou de leurs ayants droit.

Analysis of EPT and SATRAM data for the assessment of the use of radiation monitor data for space weather purposes

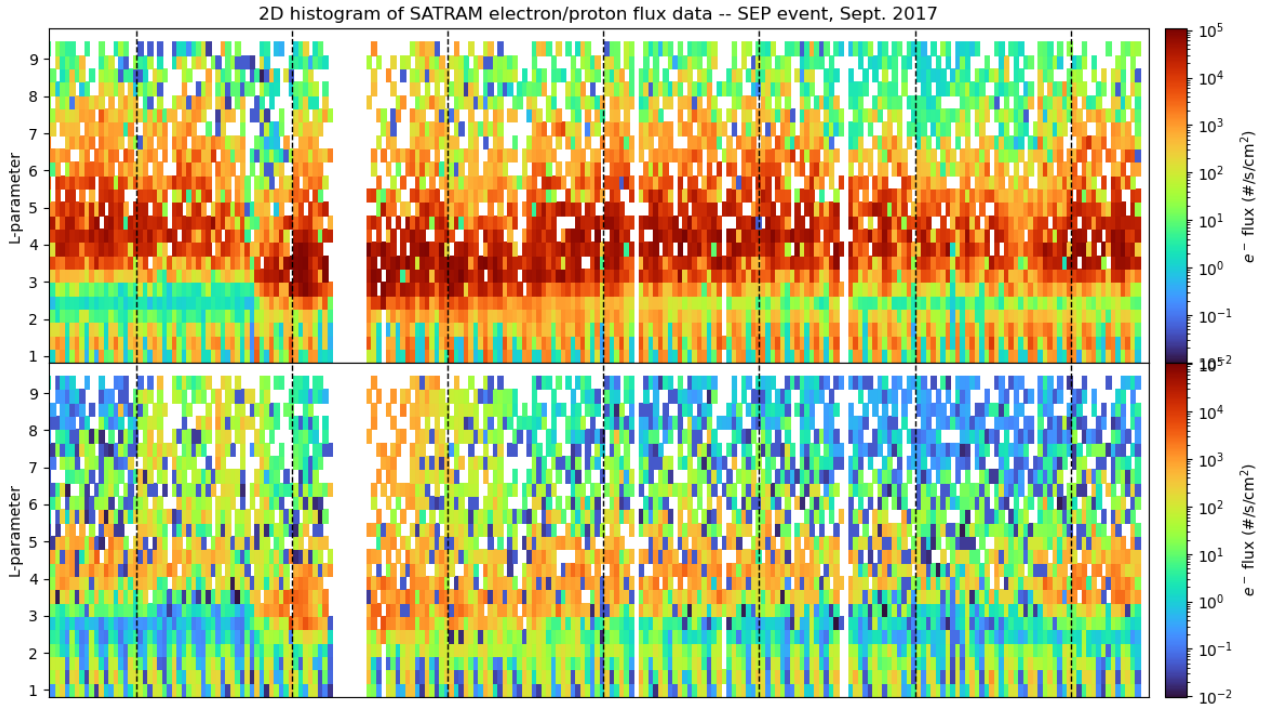

by

Owen Higgins

Master in Space science, Research focus

Supervised by:

Prof. Véronique M. Dehant (Observatoire royal de Belgique)

Prof. Denis Grodent (Université de Liège)

August 2021

Abstract

Science-class particle spectrometers such as the Energetic Particle Telescope (EPT) provide detailed measurements of particle flux and energy spectra which are necessary for studies of space weather and its causes and effects. Radiation monitors are very common instruments record basic radiation flux and dose rate statistics, normally used to warn of hazardous conditions in space. Despite their relatively inexpensive deployment and resulting widespread usage, such monitors are rarely regarded as science instruments; the Space Application of Timepix-based RAdiation Monitor (SATRAM) is one project which examines this possibility. SATRAM and EPT are both deployed on the PROBA-V satellite, meaning their data products can be directly compared – this work sets out to do that. The necessary conditions for side-by-side comparisons of the two instruments are established, and methods for visualising the data and comparing it qualitatively are developed. A detailed examination is made of the observed differences between the flux measurements of the two telescopes, including calibration factors to help mitigate these differences and potential sources of error which could be resolved by future work. Finally, two case studies of space weather events are presented, demonstrating how each instrument differs but is effective in recording such events. It is shown that EPT and SATRAM already have workable complementarities. In addition, suggestions for future improvement of the processing techniques are given, which arise from the direct comparison of the two instruments.

Acronyms

CME	coronal mass ejection
D3S	Distributed Space Weather Sensor System
ESA	European Space Agency
EPT	Energetic Particle Telescope
FOV	field of view
GOES	Geostationary Operational Environmental Satellite
MULASSIS	Multi-Layered Shielding Simulation
NASA	National Aeronautics and Space Administration
PC	physical channel
PROBA-V	PRoject for On-Board Autonomy–Vegetation
SAA	South Atlantic Anomaly
SATRAM	Space Application of Timepix-based RAdiation Monitor
SEP	solar energetic particle
SPE	solar proton event
SPENVIS	SPace ENVironment Information System
SREM	Standard Radiation Environment Monitor
VC	virtual channel

Table of Contents

1 Preface

This project, undertaken between September 2020 and July 2021, concerns the particle-detecting instruments EPT and SATRAM, comparing their data products and using them in concert to examine magnetospheric events. The motivation for the work is the prevalence of radiation monitors of a similar class to SATRAM in space, on-board various types of satellites and space vehicles, compared to more advanced instruments on the level of EPT, which are specifically designed for space physics investigations.

SATRAM is a radiation monitoring experiment that makes use of the Timepix pixel detector chip, a generalised radiation monitor used previously for scientific and industrial applications, including use in space [Granja *et al*. 2016]. It provides direct readings of radiation dose, and indirect measurement of the particle flux by means of image analysis techniques. The experiment's objective is to investigate how such a radiation monitor can be used to measure the flux of particle radiation in space. On the other hand, EPT is a space radiation spectrometer, specifically designed for science-class investigations of the radiation environment including recording flux-energy spectra, studying particle distributions in the radiation belts, validating radiation models and others. Both instruments were launched on the PROBA-V satellite in May 2013, and so sample the same space environment.

This thesis will outline some scientific background on space weather and on space radiation monitoring by instruments like SATRAM and EPT, before detailing the instruments themselves, their parameters and data products, and the work that was done to intercalibrate their results so as to be able to make reasonable comparisons between them. The results of comparisons, focusing on a couple of space weather events, are then presented. Finally, conclusions and possible directions for future work are given.

1.1 Objectives

The overall objective of this work was cross-comparison of SATRAM data to EPT, in order to get an idea of the former's capabilities and its potential use as a complement to a science-class spectrometer. This involved first acquiring a familiarity with spectrometers and radiation monitors in general, and EPT and SATRAM in particular; then comparing their data products and verifying intercalibration between the two. The desired outcomes included information about the output measurements of each instrument, especially as compared to

the other, and any calibration factors relating them which could be relied on for future investigations. A secondary outcome was the production of a set of scripts for the processing and comparison of EPT and SATRAM data, also for further development and re-use.

2 Background

As an introduction and to motivate the later discussion of methods and results, the question should be asked: why is it important to improve our understanding of space physics, and space weather specifically? Just as terrestrial weather changes all the time and determines a large part of our lives, so does space weather. The effects that inclement space weather can have on our industry, our scientific endeavours, and our very health are significant. To avoid and adapt to them, we must understand them precisely, on a theoretical and an empirical level.

Precise and scientific understanding of the physics of our space environment enables us to link the space weather hazards that affect us, to determine which phenomena cause those hazards and understand how they do so. Understanding those phenomena requires an account of the space environment: the plasma, magnetic fields, electromagnetic waves and energetic radiation that impacts Earth every day. With this understanding, it's possible to create long-term models and forecasts, or short-term warnings and alerts, which make it possible for us to account for those space weather phenomena.

In turn, creating reliable models and forecasts requires data – accurate measuring and real-time recording of space weather properties, e.g. particle flux and magnetic field strength. Ensuring the integrity of this data is therefore critical to its usefulness, and that necessitates building and verifying robust scientific instruments and satellites, with good calibration and checking. This work will form a small part of that verification, enabling further and future study of the space weather that will impact us more and more in the future. To that end, some of the relevant ways in which space weather works and affects us are outlined in this chapter.

2.1 Space weather

As the atmosphere of the Earth experiences weather – disturbances and events like rain, storms, wind and hail – so too does the space surrounding the Earth experience variation and disturbances in its conditions. By analogy we call these *space weather*. Both kinds of weather are ultimately related to the Sun, but the types of solar energy and radiation which cause and influence space weather are much different to those that cause terrestrial weather. The solar wind, the current of particle radiation continuously emitted by the Sun which washes over the Earth, is the greatest contributor to space weather. [Moldwin 2008 p. 2] The space environment extends much further than Earth's domain, of course, but in practice we are primarily concerned with the effects of space weather on terrestrial activities and on our space probes and satellites, so here the focus is on space weather that affects the Earth.

In general, space weather is caused by the interaction between the heliosphere and the Earth's upper atmosphere. The former contains the solar wind, that is a plasma of charged particles (mostly electrons, protons and helium ions) that are able to escape the Sun's gravity, and the solar magnetic field, which is pulled out from the Sun by those magnetised particles [Moldwin 2008 pp. 38-39]. The latter includes the ionosphere in its upper layers, where solar radiation creates large numbers of charged ions, and above which the magnetosphere begins [Moldwin 2008 p. 50]. The magnetosphere, defined as the region in which charged particles are affected by the Earth's magnetic field, deflects and captures the solar wind, and the ionosphere is affected and disturbed by the solar radiation. The changing activity of the Sun, encompassing the speed and direction of the solar wind, the cycle of sunspots and magnetic activity, and the occasional solar storms and coronal mass ejections (CMEs), induce changes in these regions which become the space weather phenomena that ultimately affect us.

2.1.1 Structure of the magnetosphere

The magnetosphere stretches many Earth radii away from us, to the point in space where it matches the heliosphere in strength (called the magnetopause). Its inner part, inside an altitude of about 6 Earth radii, is where space weather affects us most significantly as most satellites orbit within the inner magnetosphere. It contains charged particles that are trapped in a few distinct regions, and can be affected by solar conditions.

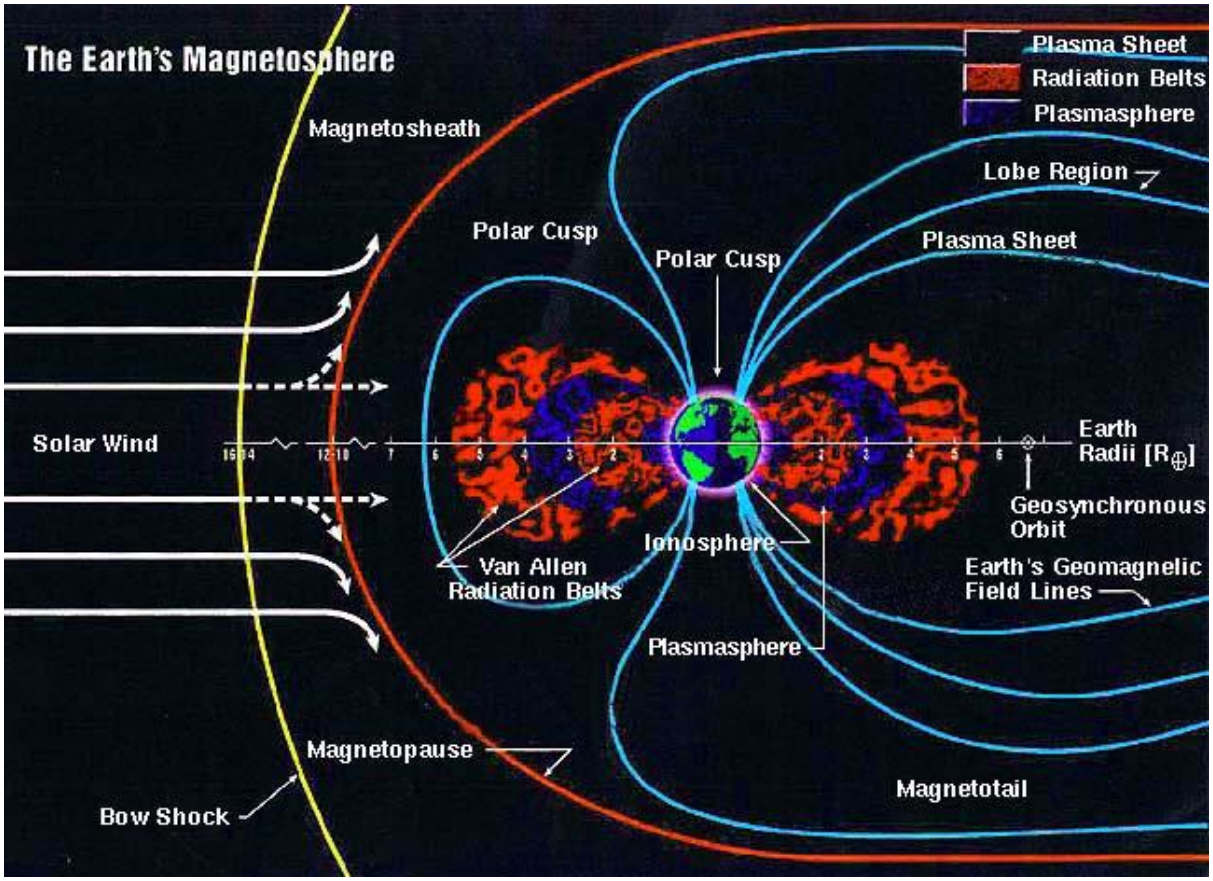

Figure 2.1: Schematic diagram of the magnetosphere. The ring current occupies altitudes comparable to the plasmasphere and outer radiation belt. [NASA]

A schematic view of the magnetosphere is shown in Figure 2.1. Innermost is the plasmasphere, a reservoir of low-energy, slow-moving ions that have risen up from the ionosphere beneath. Above and sometimes overlapping it, the ring current is a flow of medium-energy electrons and protons that drift around the Earth in opposite directions. The flow gives rise to an electric current due to the particles' opposite charges, and this ring current in turn generates a magnetic field that opposes the Earth's internal magnetic field. Overlapping with those is found the Van Allen radiation belts, two distinct belts of trapped, charged, high-energy particles separated by an empty "slot" region. The inner belt overlaps the plasmasphere; it contains electrons and energetic protons, the latter of which dominates the flux (so that it is sometimes called the proton belt) because they are trapped by the comparably stronger magnetic fields. The outer belt is much larger, and with a weaker B-field contains mostly only electrons. Both harbour deadly amounts of hard radiation, both for satellites and prospective astronauts.

The form or shape of the radiation belts is due to the movement of the particles within it. The charged particles largely follow magnetic field lines which keep them trapped in the

belts; the interaction with the magnetic field makes them gyrate around the lines [Moldwin p. 66]. The field lines extend from the polar regions, so particles follow them north or south until they reach the regions of high magnetic field strength and are bounced back, owing to conservation of their magnetic momentum, at the so-called mirror point. The slot region exists due to the loss of particles into the ionosphere [Moldwin 2008, p.55], as a result of electron interactions with electromagnetic waves called "whistlers". Finally, electrons and protons drift around the Earth in opposite directions due to their opposite charge, electrons moving eastwards and protons west [National Observatory of Athens 2012], as visualised below.

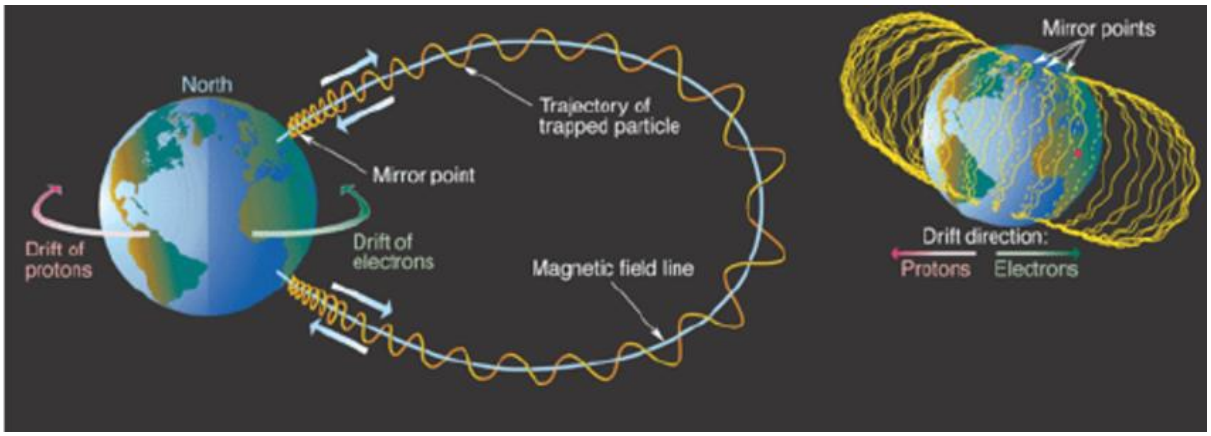

Figure 2.2: Motion of particles in the Earth's magnetic field. [Anagnostopoulos et al. 2010]

2.1.2 Solar wind interactions

This section largely follows Moldwin's book, chapter 4.5 [2008, pp. 54-57]. As mentioned, the Earth's magnetosphere deflects and captures particles from the solar wind. The basic interactions between the magnetosphere and the solar wind are that the magnetopause is compressed by the pressure of a stronger solar wind and expands against a weaker one, and that the magnetotail is produced by the wind's force. The fact that the solar wind carries a magnetic field means that the two interact - the magnetic field near to Earth is a combination of the field emanating from the Sun, carried by the solar wind, and Earth's internal field. Earth's internal field doesn't change, at least not on timescales that affect us, so the combined field only changes as a result of solar activity affecting the Sun's B-field. Magnetic reconnection is one of the primary ways that this happens. When magnetic fields pointing in different directions (i.e. that go north-south as opposed to south-north) come into contact, the separate field lines merge into one. In the case of field lines

moving from the Sun over the Earth's magnetosphere, closed field lines which run from pole to pole are pulled open to *connect* with the Sun's field line, at the magnetopause. In Figure 2.3, this is indicated in the first red region. Notice that reconnection depends on the solar magnetic field pointing southward, which it does not always do, or not to the same degree.

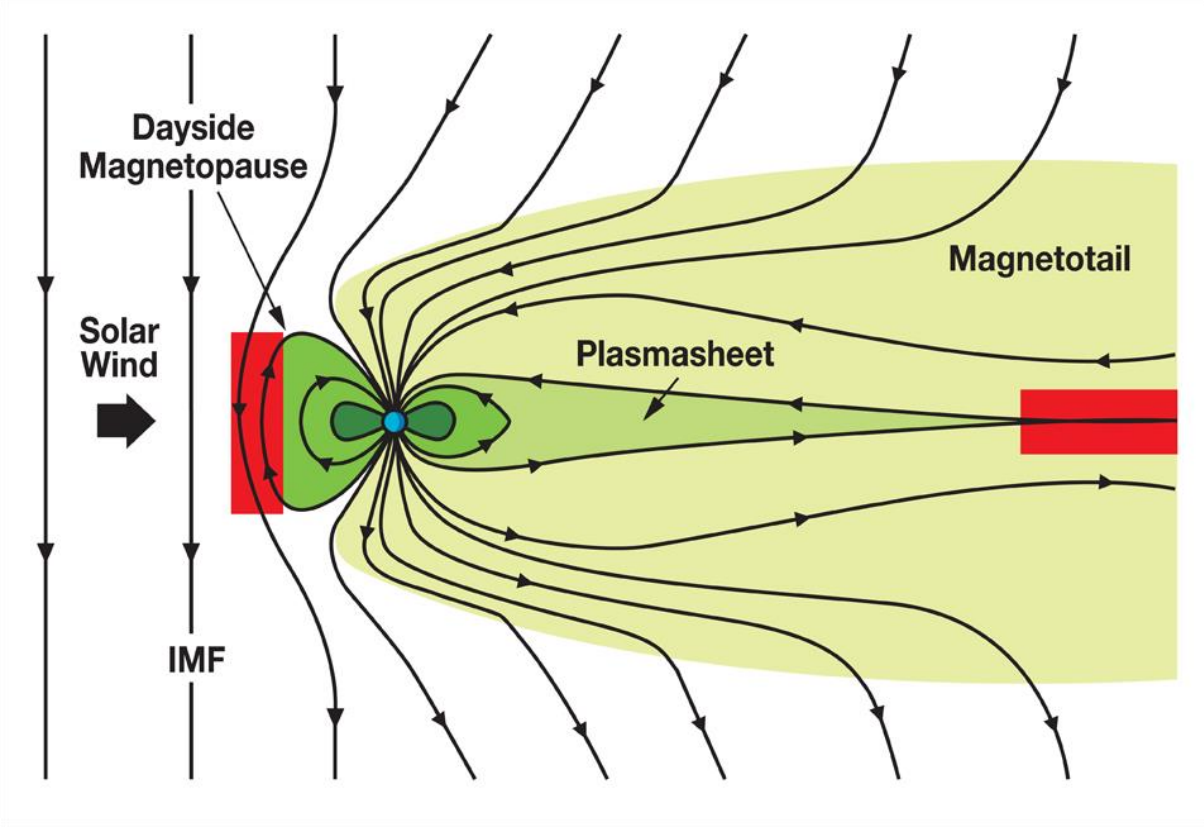

Figure 2.3: Magnetic reconnection: the field lines around Earth are "pulled" open and back, until they separate.

The charged particles of the solar wind create an electric current over the magnetic field, which moves the field lines in towards Earth again in the magnetotail. This is referred to as convection and is another main effect that the solar magnetic field has on Earth's. At the back of the magnetotail, convection presses field lines together from above and below, whereupon they reconnect with each other again, disconnecting from the solar wind, which carries on. They go back to being connected from pole to pole as "closed" field lines. Thus the cycle of reconnection can continue.

The reconnection of magnetic field lines can release an enormous amount of energy, which is largely imparted into the charged particles carried by the field as kinetic energy. Reconnection is mainly the cause of geomagnetic substorms, which are common during larger space weather events. Solar storms which affect the flow of the magnetic wind and

increase the pressure that it puts on our magnetosphere are, along with the particles that comprise the solar wind themselves, the main driver of space weather events.

2.1.3 Space weather phenomena

Of those such events which come close to affecting us on the Earth, two are important to highlight: geomagnetic storms in the magnetosphere, and solar energetic particle events from the Sun.

Solar energetic particles (SEP) are generically charged particles - (protons, electrons and heavier ions) - which come from the Sun: the whole solar wind is made of them. They contrast with cosmic rays, the other source of such charged particles, which are typically galactic and extragalactic in origin. SEP events are marked by a much higher intensity and/or flux of these particles. Solar flares or other shocks can accelerate protons to such high energies that they can penetrate into the upper radiation belt and beyond, known as a solar proton event (SPE). High numbers of energetic protons can be damaging to satellites and airborne activities, as they are massive particles and constitute hard radiation when having sufficient energy. They can in extreme cases pose harm to aeroplane pilots and passengers through increased radiation [Wilson *et al*.], contaminate astronomical images much like cosmic rays, and damage spacecraft with excess electric charge. The latter can also be seen in the South Atlantic Anomaly (SAA), a region where part of the inner radiation belt comes close to the Earth, exposing spacecraft that travel through it to increased particle radiation, especially protons. (Figure 4.8 shows the SAA's location on a map of global electron particle flux.) They can even harm astronauts: in 1972, a historically strong SPE occurred, right around the time of the Apollo moon missions. If astronauts had been on the moon at the wrong time, they could have received fatal radiation doses [Moldwin 2008, p 101].

Another type of SEP event is the coronal mass ejection (CME). When magnetic pressure builds to sufficient levels, the Sun's magnetic field will reconfigure, throwing a portion of it off into space along with huge quantities of solar plasma. The CME is one of the main causes for geomagnetic storms over Earth. When a coronal mass strikes Earth, it compresses the magnetosphere and pushes back the magnetopause, which causes mass magnetic reconnection there and, later, in the magnetotail. The start of the storm, called the commencement, is marked by surface electric currents amplifying the magnetic field. As the CME passes over and past Earth, the reconnection moves to the tail, releasing massive

amounts of energy in the form of high-energy plasma, which is transmitted to the ring current. As mentioned above, the ring current induces a magnetic field which opposes the terrestrial one. The storm ends as this current eventually weakens, which can have a “decay time” of days or weeks. [Moldwin 2008, pp. 59-60.]

The effects of a geomagnetic storm are significant: with a decreased magnetic field strength, radiation and charged particles from the Sun can penetrate further into the magnetosphere than usual. Solar energetic particle events can cause the same hazards even more directly. Depending on how powerful the event is, they can result in danger or damage to satellites from exposure to the strong radiation or charged particles: flipping bits, degrading solar panels, inducing short-circuits or even power surges in the circuit boards, similar to a lightning strike. Even just the kinetic effect of increased solar wind decays the orbits of low-Earth orbiting satellites, pushing them closer to re-entry over the course of years [Moldwin 2008, p. 82]. In extreme cases the solar activity can penetrate very close to the Earth’s surface, inducing destructive currents in electrical power grids, degrading telecommunications infrastructure, or even exacerbating corrosion in long pipelines. Strong geomagnetic storms have historically caused blackouts such as the storm of 1972 mentioned above which damaged infrastructure in North America [Moldwin 2008, pp. 80-89]. Such problems are not new, either: the legendary Carrington Event in 1859 caused sparking on the then-standard telegraph networks and set some offices on fire; had it occurred today, it would cause widespread disruption [Phillips 2014].

2.1.4 Magnetic field indices

The strength of the magnetic field as correlated with the strength of solar activity and geomagnetic storms, can be characterised by magnetic indices. Two important ones are Dst and Kp. Dst, or the Disturbed Storm Time index, measures the deviation of the magnetic field (at level of the ring current) from the hourly average. Negative values of Dst correspond to decreases in the magnetic field, which represent increases in the ring current and its corresponding magnetic field, and vice-versa. Since the ring current is so dependent on solar activity and correlates with geomagnetic storms, Dst is a useful indicator of space weather intensity. The commencement of a solar storm is easily seen by an increase in Dst, followed by a sharp decrease due to the ring current, then a slow recovery.

Kp is a logarithmic scale which measures the variability of the magnetic field: it is determined by measuring the range (difference between the highest and lowest values) of disturbance of the magnetic field during three-hourly time intervals. It corresponds to the regions of the field moving inward or outwards, due to geomagnetic storms [Moldwin, p.60] [National Oceanic and Atmospheric Administration] - the more turbulent and disturbed the field is, the higher Kp gets, on a 1-9 scale. (It has an average value of 3, and also decreases when the field is calmer than average.)

2.1.5 McIlwain's (*B, L*) coordinates

Rather than using geocentric coordinates, which do not line up with the magnetic field as its dipole is tilted and slightly shifted with respect to the Earth's rotation axis, the extent of the magnetosphere can be described in magnetic (*B, L*) coordinates. In simple qualitative terms, the McIlwain L-parameter (*L*) represents the distance (expressed in Earth radii) between the centre of the Earth and the point where a magnetic field line crosses the magnetic equator. For example, a field line with $L = 2$ can be thought of as being 2 Earth radii from the centre of the Earth at its widest point. That same line will come closer and closer to the Earth as it approaches the polar regions, so the altitude would decrease, but the L-parameter remains the same. Charged particles in the magnetosphere can be tracked by their L-coordinate, because particles that are trapped by the magnetic field follow the magnetic field lines and have a constant L-parameter as they do. This parameter can be used to characterise field lines, and hence features of the magnetosphere, regardless of latitude. B is the magnetic field strength as measured at the mirror point, where the particle bounces back from the polar regions. Since the magnetic field is strongest near the poles, and weakest at the equator, it complements the L-parameter by giving a magnetic description of latitude. The inner Van Allen radiation belt occupies the region of $1 < L < 2.5$, the slot region extends for about $2.5 < L < 3$, and the outer belt is present from $L > 3$ up to $L = 8$ or 9 - depending on the space weather conditions.

2.1.6 Differential flux vs. integral flux

When tracking space weather and its effects, one of the primary quantities to be measured is the radiation flux - i.e., the amount of charged particles passing through a region of the magnetosphere, per second, per unit area, per unit solid angle. Typically the

flux is discriminated by particle type (between light particles such as electrons and heavier particles such as ions), but it can also be separated by particle energy, most often in units of MeV. Therefore we have to distinguish between differential and integral flux here.

Essentially differential flux depends on the particle energy, while integral flux is independent of it. Differential flux is obtained when particle flux is separated into energy bands of a certain width in MeV and around a certain central energy. For example, one may wish to record low-energy protons of 1-2 MeV separately from higher-energy protons of 2-8 MeV, and separately from high-energy particles with > 8 MeV. The data obtained from doing this comes in three channels, none of which represent the full energy spectrum of the radiation environment (proton radiation, in this case), but only portions of it. A reason that this arises is that you may have multiple detectors which are sensitive only to particular energy ranges, but want to record a full spectrum - this is the case with EPT, as will be shown later.

Formally, integral flux is obtained just by integrating over all possible energies. For flux above some starting energy E_0, this looks like

$$\phi_{int}(E > E_0) = \int_{E_0}^{\infty} \phi_{diff}(E)\, dE$$

Equation 1

where ϕ_{diff} is a flux in units of particle counts per unit time, per unit of detector area, per unit of solid angle of the sky, per unit of particle energy. Those units are seconds, square centimetres, steradians and megaelectronvolts respectively, so the units are written more compactly as #/s/cm^2/sr/MeV. This form will be used throughout the work for further equations.

With discrete flux measurements, as will be the case for a particle detector, Equation 1 can be done as a discrete sum instead. One sums over the data in all energy bands, weighting each by its width in MeV, to obtain the integral flux. This procedure is developed further alongside the methods.

2.2 Monitoring space weather

With the many components of the Earth's near-space environment which can contribute to space weather events, and the considerable effects that those events can have on human activities both in space and on the ground, it is critically important to both

understand the mechanisms that drive it, and keep a close eye on its day-to-day variations. Spacecraft and aircraft have radiation monitors and magnetometers to inform their operators of any dangers to them; many telescopes and instruments exist specifically to examine the magnetosphere and the heliosphere, near to and far from Earth. The two instruments which are a focus of this work are a continuation of that practice, so here some context is given for their development.

2.2.1 Types of space weather missions

The very first satellites to be launched were ones which studied the regions where space weather occurs near Earth. Sputnik in 1957 investigated the ionosphere, while the Explorer satellites in 1958 confirmed the existence and properties of the radiation belts, causing them to be named after the missions' designer, James Van Allen. Many other probes were launched to characterise various parts of the Earth's magnetosphere during the 20th century: the OGO satellites were among the first to investigate the Earth-Sun relationship in the 1960s. Missions to study space weather events in particular came in more recent years, as the proliferation of satellites prompted systematic study of its effects [National Academy of Science 1997, p.2]. The recent NASA Van Allen probes (2012-2019) were a dedicated mission to study the radiation belts and ring current, aiming to understand their dynamics during geomagnetic storms. NASA's GOES series of satellites are primarily meteorological but include space environment monitoring instruments and report regular space weather data. The NASA-ESA STEREO satellite monitors the Sun for evidence of coronal mass ejections. In the last decade ESA began a space weather monitoring programme including its Distributed Space Weather Sensor System (D3S), aiming to have multiple sensors observing the Earth-heliosphere interaction at any given time. [Kraft *et al*. 2019] Such satellites include dedicated instruments designed to investigate some particular aspect of the space environment.

Instruments like the Van Allen probes, as well as being tailored to specific scientific ends, are deployed on specific and often short-term missions to achieve those goals. The earlier space weather missions were invariably of this type, as researchers aimed to establish the principles of the field, to outline the specific space phenomena, and learn its effects on spacecraft. More recent missions which have arisen, such as those of the GOES and D3S programmes, are of the newer class of long-term and continuous space-weather

monitoring. Such missions are no longer focused on learning what space weather's effects are, but rather to predict where and when these effects will occur, so that they can be fully accounted for in the design and operation of unrelated space missions. This is analogous to how terrestrial weather forecasts are used and represents progress in the field.

Meanwhile, many satellites both commercial and scientific have carried general-purpose radiation monitors, ever since it was known that radiation conditions in the Earth's vicinity could be damaging to space equipment. These instruments typically measure the dose of ionising radiation or the incidence of high-energy particles. This information is used to help satellite operators analyse equipment failures or errors which may be caused by charged particles, post facto. Such detectors also feature on aeroplanes flying polar routes and spacecraft such as the International Space Station. The Standard Radiation Environment Monitor (SREM) is an example of such an instrument, developed for ESA around 2000 as a piece of standardised, low-cost equipment which could be added to many satellites for consistent radiation monitoring. It can be seen therefore that a radiation monitor is typically an ancillary device to the main purpose of a space activity, not a primary instrument as with the space weather satellites mentioned above. However, once so many radiation monitors were placed in orbit, already returning data to the Earth, they came to be used for space weather research as a secondary function. One of those research purposes is to characterise the space radiation environment, for the objective of creating and updating models of radiation in space and the upper atmosphere. Radiation monitors as deployed on existing air- and space-craft provide data sources for the development of these models, such as with NASA's NAIRAS. [Mertens *et al*. 2009]

2.2.2 Space weather instrumentation

The differences between satellites with instruments specifically designed and intended to study the radiation environment, and satellites with ancillary radiation monitors, can be seen in the design of those instruments. [Cyamukungu *et al.* 2014] Modern scientific instruments for detailed radiation belt study are particle spectrometers; that is, they measure the flux of charged particles to obtain an energy-flux spectrum. They are designed with a particular science objective in mind. For this purpose, they have a good ability to discriminate between particle types (electrons, protons, and heavier ions of various energies) and to determine the absolute energy of those particles, but they are larger

instruments requiring a greater power budget on a satellite platform. Examples include the instruments on the Van Allen probes, such as magEIS and HOPE.

Radiation monitors by contrast are smaller, lighter, and cheaper to use, but less capable. They don't directly obtain particle fluxes and are limited in their ability to distinguish particle types, but can still do this. Often the main quantity they output is radiation dose, obtained by measuring energy deposited in the volume of the monitor and the count-rate of all particles, as their purpose is radiation safety and warnings. SREM and the newer NGRM are examples of standard radiation monitors for spacecraft [Hadjas 2016, p. 4] from which particle fluxes are deduced within some limitations; Timepix is a radiation monitor chip that has been used for both space-borne and terrestrial applications. Its initial objective was dosimetry, and its uses have later been expanded, as in the SATRAM experiment.

New instruments are continually being developed to better characterise and monitor the space weather environment. The instruments involved in this work, EPT and SATRAM, are examples of a modern particle spectrometer and a radiation monitor, respectively. Both are onboard PROBA-V for in-orbit technology demonstration and can be used for the purpose of space weather monitoring. One of the important aspects of this work is determining how well the two types of instrument can work in conjunction, simultaneously giving complementary measurements of the same space weather phenomena. This is presented in the following chapters.

3 Instrumentation and methods

This project aims to evaluate the use of advanced radiation monitor data, as that from SATRAM, in detailed space weather surveys. This will be done through comparing the capabilities and output of SATRAM with EPT, so a precise account of the two instruments - their properties, how they behave, their technical commonalities and differences - is important to make as a basis of this analysis. This chapter first outlines the operation of EPT and SATRAM, then discusses the work done in analysing and comparing data from each instrument to ensure that their results are in good agreement. Afterwards the methods used to investigate space weather events are developed.

3.1 PROBA-V

PROBA-V is an ESA mission launched in May 2013, named **PRoject for On-Board Autonomy–Vegetation**. PROBA-V is the third in the PROBA series of satellites, and as the name suggests its purpose is primarily to monitor vegetation growth. That mission was officially ended in 2020, although the satellite is still functional. [European Space Agency b] A few other in-orbit demonstration instruments are included on the satellite, EPT and SATRAM being two of them.

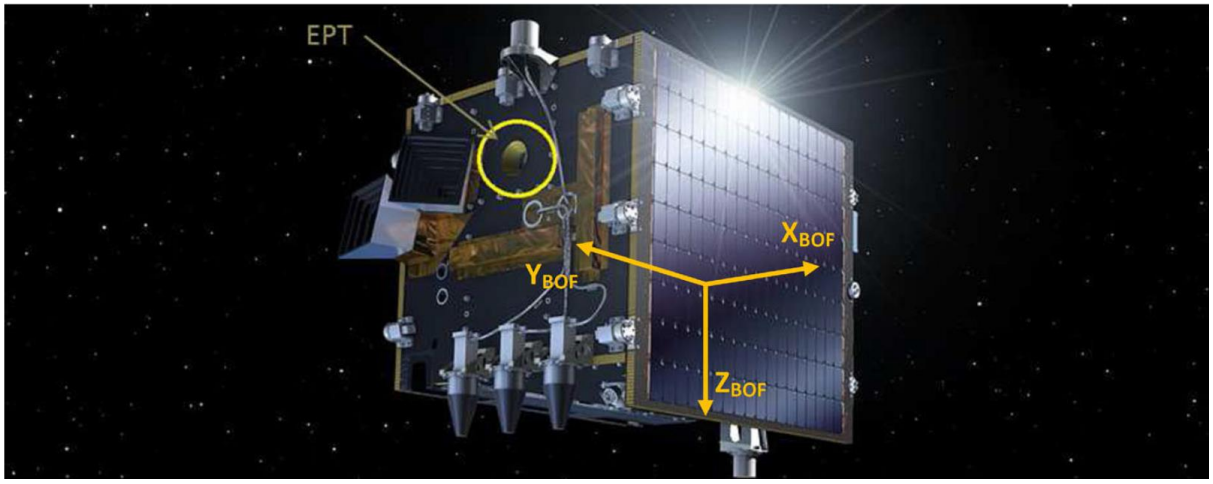

Figure 3.1: The PROBA-V satellite with EPT aperture marked. SATRAM is located on the opposite side.

PROBA-V is a cube-shaped satellite 0.64 m^3 in size [Francois *et al.*, pp. 4], 3-axis stabilised so that its vegetation instrument always points towards the Earth. EPT and SATRAM are positioned so that in this configuration, both look in opposite directions. On the day side of Earth, EPT faces west and SATRAM east; on the night side these are

reversed. The satellite itself is positioned in a Sun-synchronous, low-Earth orbit of altitude 820 km, and with an inclination of 98.7°. [Cyamukungu *et al.* 2014] With an orbital period of just over 100 minutes [European Space Agency c], processing over the Earth as it goes, PROBA-V completes about fourteen orbits a day. For EPT and SATRAM it collects data at all times giving coverage of the planet's entire surface, except for a band going from the north African coast to the north of the UK, where the acquisition is stopped for about ten minutes time to downlink data to the control centre in Redu, Belgium. The polar regions above 82 degrees of latitude are also not covered due to the 98.7° inclination of the satellite's orbit. This gap in observations is present in both EPT and SATRAM data, but is geographically minor.

3.2 EPT

EPT is the Energetic Particle Telescope, a science-class instrument developed as a technology demonstration. It intends to produce results and data products comparable to other science-class radiation spectrometers, such as instruments on the Van Allen probes, while using less resources (mass, electrical power, volume) than traditional instruments. [Cyamukungu *et al*. 2014, p. 2] Central to its design is the dependence on on-board signal-processing techniques for particle identification and classification.

The instrument is a charged particle spectrometer which detects and classifies particles from the radiation environment. It registers the identified energetic particles in so-called "physical" channels, and their incident energy spectrum is obtained by unfolding these particle counts. It is a medium-sized instrument, just about 4 litres in volume, but a further-miniaturised version mEPT is in development as a successor.

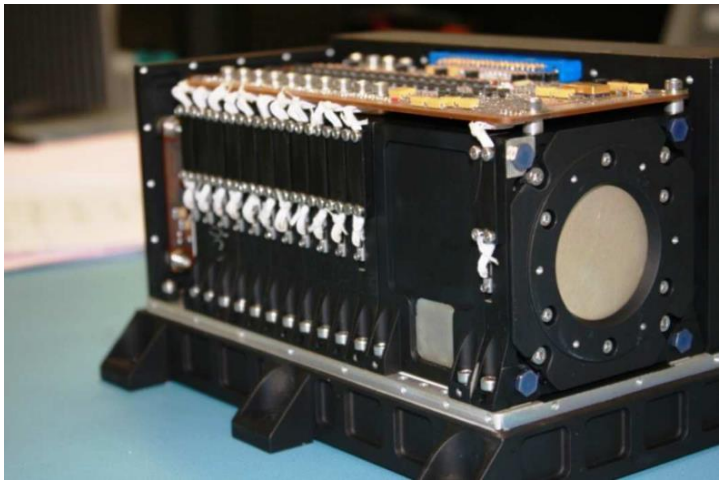

Figure 3.2: The Energetic Particle Telescope, with cover removed. [Cyamukungu et al. 2014]

The detector assembly, shown in Figure 3.3, consists of two concentric, analogue sensors at the front of the telescope aperture (called S1/S3), a collimator, one further analogue sensor slightly behind them (called S2), and ten digital detectors lined up behind that (D1-D10). The front sensors define the angle of incoming particles and collect low-energy particles. Being analogue sensors, they precisely measure[1] the amplitude of the incoming signal, which is used for particle separation or definition of energy channels. The back, digital detectors collect high-energy particles. The particle type is discriminated by the analogue sensors, while the energy is given by the last digital detector hit. Essentially the EPT instrument is a directional particle spectrometer, with a maximum field of view of 52°.

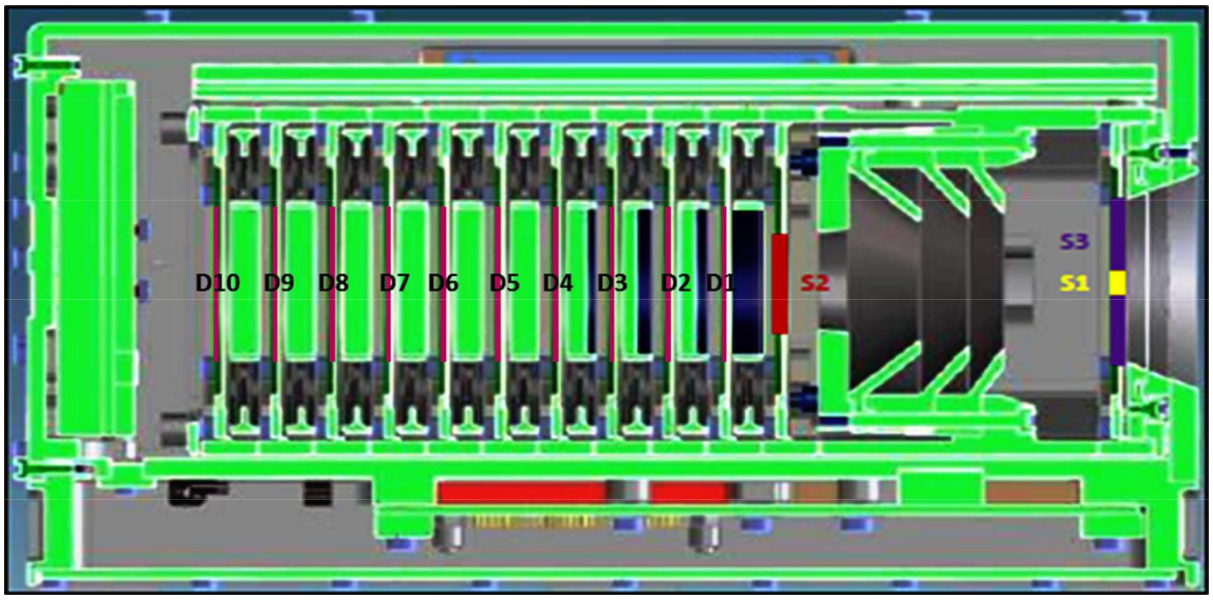

Figure 3.3: EPT cross-section, analogue sensors S1-S3 and digital detectors D1-D10 labelled. [Cyamukungu et al. *2014]*

Incident particles are counted and are classified into various channels, according to the identified particle type (e^-, p, He^+, or heavier ions) and the range of energies. The incident energy is captured by the *physical channels* or PCs, which count particles during a given integration time and combine the information about each particle's type[2] and the last digital detector that it hits. The real energy is represented in the output data by a *virtual channel* or

[1] They measure the signal up to 4095 ADC units, using a 12 bit analogue-to-digital converter (ADC) that is setup in a way to be able to measure fully the highest energy deposition from He ions that can be registered by the instrument, where the digital detectors measure only "hit" or "not hit" (1 bit).

[2] In the case of EPT, there is no significant mixture of particles in the channels. Some discrimination capability was however lost due to an incident in June 2014 [Borisov et al. 2019], resulting in higher noise and lowered gain in the analogue sensor S3.

VC, which covers a range of energies. Each physical channel is responsive to a number of virtual channels.

Each physical channel can collect particles from every virtual channel (= energy range), with a different efficiency of detection for every PC-VC pair. Where the efficiency from a VC is zero or close to it, the PC won't collect any particles. In other words, fluxes from different VCs contribute (with corresponding efficiencies) to the count rate in a given PC. The VCs are defined such that each PC is only significantly sensitive to a few VCs, with one VC dominating the response; this means that every PC can be uniquely identified by its VC response. By knowing each efficiency value it is possible to construct a system of relations between the PCs and VCs[3], which makes it possible to reconstruct the VC information later when the instrument is flying, based only on the count-rate in PCs. The efficiency values were computed for EPT based on GEANT4 simulations and verified with beam tests done on-ground. [Cyamukungu *et al*. 2014] [Borisov *et al*. 2014]

The unfolding procedure amounts to calculating what energy flux in the virtual channels is represented by the counts in the physical channels, using the efficiency matrix that has been calculated through GEANT4 simulations. These energy fluxes, given separately for each of the virtual channels, are the data which is finally considered. To illustrate the data handling, I will focus on electrons here. They are recorded in the virtual channels given in table 3.1.

Number	Start	Midpoint	End	Width
00	0.5	0.55	0.6	0.1
01	0.6	.65	0.7	0.1
02	0.7	0.75	0.8	0.1
03	0.8	0.9	1.0	0.2
04	1.0	1.7	2.4	1.4
05	2.4	5.2	8.0	5.6

Table 3.1: EPT e^- virtual channels. Units for each column are MeV, except Number.

[3] The equations relating every VC to each PC are arranged into a matrix equation that simply multiplies a matrix of all efficiency values by the vector of VCs to get the PCs. Tables showing this are given in Cyamukungu et al. [2014].

In the processed, output EPT data files, each of these fluxes is given as a separate column. For example, the column `e-fl-00` contains the total electron flux collected since the last integration, from electrons which entered the detector with an energy between 0.5 and 0.6 MeV. As can be seen, particles with energy below 0.5 MeV are not recorded.

Each of these channels / columns is a record of differential energy flux, with the units counts/s/cm^2/sr/MeV. It is convenient to obtain an integral flux through the detector, which can be done by essentially summing together each of the energy channels, multiplied by their widths in MeV. The formula for this is (following on from section 2.1.6):

$$\phi_{int}(E) = \sum_{i=1}^{n} \phi_{diff}(M_i) \times W_i$$

Equation 2

for n channels, where M_i is the midpoint of channel i, W_i is its width, ϕ_{diff} is a function of M_i and channel 1 has start energy $S_i = E$ MeV. That is, this formula gives the integrated flux above energy E. Appropriate values for electron data are given in Table 3.1 above.

This procedure provides a single integral flux with units of #/s/cm^2/sr. The dependence on MeV has disappeared, because each channel was multiplied by its channel width in MeV. Therefore, this is now a particle flux, not an energy flux. It is still dependent on angle (in steradians) and so is directional; this will be addressed later.

3.3 SATRAM

SATRAM is an experiment named **Space Application of Timepix-based RAdiation Monitor** - as stated, it is a radiation monitor based on a Timepix semiconductor-pixel particle detector [Granja *et al*. 2016, p. 115]. A companion instrument to EPT on the PROBA-V satellite, SATRAM is also deployed as a technology demonstration. Like EPT, it detects energetic particles; but as a radiation monitor-like instrument, it does so with a different focus and mechanics. It is close to a simple dosimeter in design: rather than detecting and classifying energetic particles which enter it, it only aims to record the energy deposited by any particles which pass through it. This deposited energy is used to obtain radiation dose, which is its primary data product.

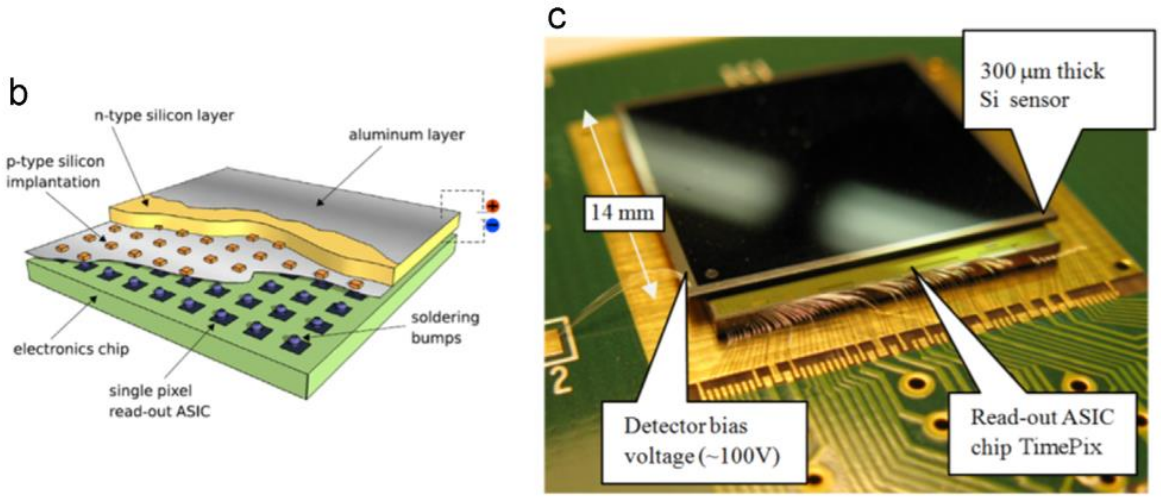

Figure 3.4: Visualisation of the composition (b) and size (c) of the Timepix chip used in SATRAM. Adapted from Figure 1 (b) and (c) from Granja et al. *[2016 p. 116]*

But SATRAM is more advanced than just a dosimeter, as it can count and classify the type and direction of particles that hit it. Unlike EPT, which has an aperture leading to a number of discrete detectors, SATRAM has one detector made of a matrix of pixels. An incoming particle will activate some of these pixels and form a trace on the detector; classification is based on the size and shape of these traces, and the energy recorded by them.

SATRAM, like EPT, divides its flux detections into channels. This is not however because of the experiment design, but due to how the Timepix detector that it uses works. The four identifiable particle types (electrons, protons, alpha particles, and heavier ions) are each grouped by the detector into two "channels": one for low-energy particles coming from any direction and high-energy particles with an incident angle <20°, and one for high-energy particles with a greater incident angle than that. Hence in total there are 8 particle classes, two for each particle type; in this work only four were used, the electron and proton channels. The reason behind this grouping is that particles hitting the detector are mainly classified by their shape. Both slow-moving particles, and fast-moving particles which hit approximately head-on, produce a roughly circular image on the detector whose size depends on the particle's ionization power. High-energy particles that hit at a significant angle will instead create a long streak as they pass through the detector (see Figure 3.5). Hence for a given particle type, this is the only distinction that it is possible to make.

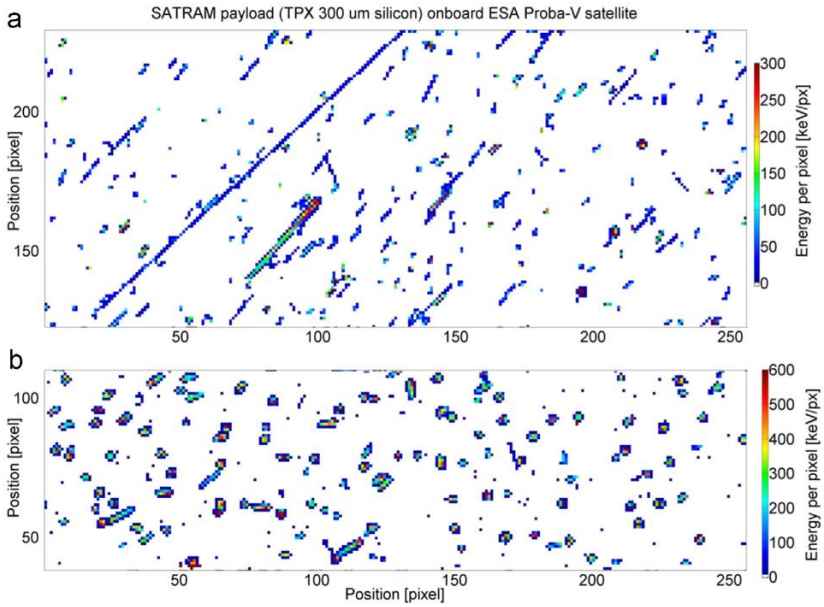

Figure 3.5: Examples of a) high-energy particles hitting at oblique angles, and b) any other particles.

The detector, a Timepix chip also used in other terrestrial contexts, cannot classify particles precisely according to their energy. It can only record and identify the high-energy part of the spectrum when incoming particles enter at a strongly inclined incident angle. It does record the energy deposited in each pixel[4], so the energy deposited by a particle corresponds to the energies recorded by a number of pixels, taken as one cluster.

As well as the shape of the trace left by the particle, which is used for primary identification, the classification algorithms used for the Timepix detector account for the direction of the particle and the deposited energy of the cluster [Granja *et al*. 2018 b, p. 66-67]. The actual classification of the particles is done offline [Granja *et al*. 2018 a, p. 144] after recorded frames are downloaded from the satellite. The exposure time for a single frame is either 0.002 seconds, 0.2 seconds, or 20 seconds. The readout time after integration concludes is about 100 milliseconds; unlike EPT, for which each measurement is 2 seconds long and comes every 2 seconds, SATRAM has a varying delay between new exposures which serves to smooth the operation of the instrument. [Granja *et al*. 2016, p. 118]

[4] When too many particles hit the detector during a given exposure (or integration time), their traces start to overlap and it becomes impossible to distinguish each particle's trace. In this case, the integration time is decreased so that readouts can clear the detector more quickly, and the detector only counts the number of particles. [Granja et al. 2016, p. 120]

The measured energy is used to calculate a radiation dose, rather than an energy flux as EPT can do. Dose, which has units of $pGy = 1 \times 10^{-12}\ Gy$ (where $1\ Gy = 1\ J/kg$), represents the energy deposited in an object per unit mass of the object. Knowing the weight and volume of the detector in SATRAM, it is straightforward to convert the deposited energy into a dose, called the silicon dose, which represents the energy deposited in the sensitive material of the detector.

One might think that given the radiation dose and the particle flux, it would be possible to obtain an energy flux by conversion. However, the instrument only gives the energy which was deposited in the detector, and not the whole energy of the particles which hit it. Incident particles, especially high-energy ones, can easily pass through the entire detector and when they do, only part of their initial energy is recorded. SATRAM's detector volume is small, and it cannot detect if a particle passed through or stopped completely in that volume. So, a majority of particles pass through the detector, and their deposited energy does not equal their initial energy. The dose rate only represents that deposited energy. This means that the particle flux can only be converted to an integral flux above a certain energy, and not to a differential energy flux, as with EPT.

Given the above properties of the instrument, the particle flux can be integrated for a particular particle type simply by summing together the two channels for that type, and this is what is done for this work. Unlike in EPT the two channels are each integral, because they cover the entire energy spectrum; they are classified only by their incident angle, where EPT alternatively classifies by energy level[5]. But when both channels are summed together, all incident directions are covered, so the resulting integrated particle flux is omnidirectional. Here, it is omnidirectional over 2π steradians, or a half-sky, as while particles could be detected if they struck the sensor from behind, they are in practice shielded by the mass of the satellite behind it. This particle flux has units #/s/cm^2.

An additional factor to be considered is that the SATRAM detector is also shielded from the front by a layer of aluminium, 0.5 mm thick [Granja *et al*. 2016, p 118], in front of the detector. This shielding will reduce the energy deposited by low-energy particles (by blocking most of them from crossing it in the first place): mostly electrons, but also lower-

[5] Some detectors can do both at once, for example PAMELA or 3DEES, but it happens that EPT and SATRAM each only use one means of classification.

energy protons, and mainly particles under 1 or 2 MeV. The shielding can block electrons with less than about 0.5 MeV of energy entirely (and also attenuates particles above that level), meaning that SATRAM has effectively the same lower limit of incident particle detection as EPT does. However, this attenuation must still be taken into account when comparing the two instruments' data.

3.4 Quantifying differences between EPT and SATRAM

One can see from the above that it should be possible to compare the particle fluxes between the two instruments, so long as all significant differences in their construction, how they operate, and how their data is processed (both on-board and by the teams receiving the data on Earth) are accounted for. The fluxes given by EPT represent the differential (per MeV) directional (per steradian) fluxes as encountered in outer space, expressed in #/s/cm^2/sr/MeV, while the fluxes given by SATRAM represent integral omnidirectional (over 2π) fluxes as encountered behind a given shielding expressed in #/s/cm^2. Given that the two detectors are quite different classes of instrument, this is however not a simple task. Primarily the two data sets must be expressed in the same units, but there are other factors as well. We consider here some of the most significant ones to obtain a first-order approximation of the comparison.

3.4.1 Shielding simulations

First, the SATRAM shielding mentioned above must be considered; it will attenuate the particle energy flux as seen by the instrument at low energies. To account for this effect, a simulation is performed of particles in EPT's energy channels passing through the shielding, and the EPT data is weighted by the proportion of particles reaching the SATRAM detector as compared to the initial population of particles. In particular, Equation 2 for the integration can be modified to:

$$\phi_{int}(E) = \sum_{i=1}^{n} \phi_{diff}(M_i) \times W_i \times P_i$$

Equation 3

where P_i represents that fraction as a number between 0.0 and 1.0, and other variables are as in Equation 2. Figure 3.6 shows this proportion for protons and electrons having energies matching EPT's channels (as shown in Table 3.1 for electrons).

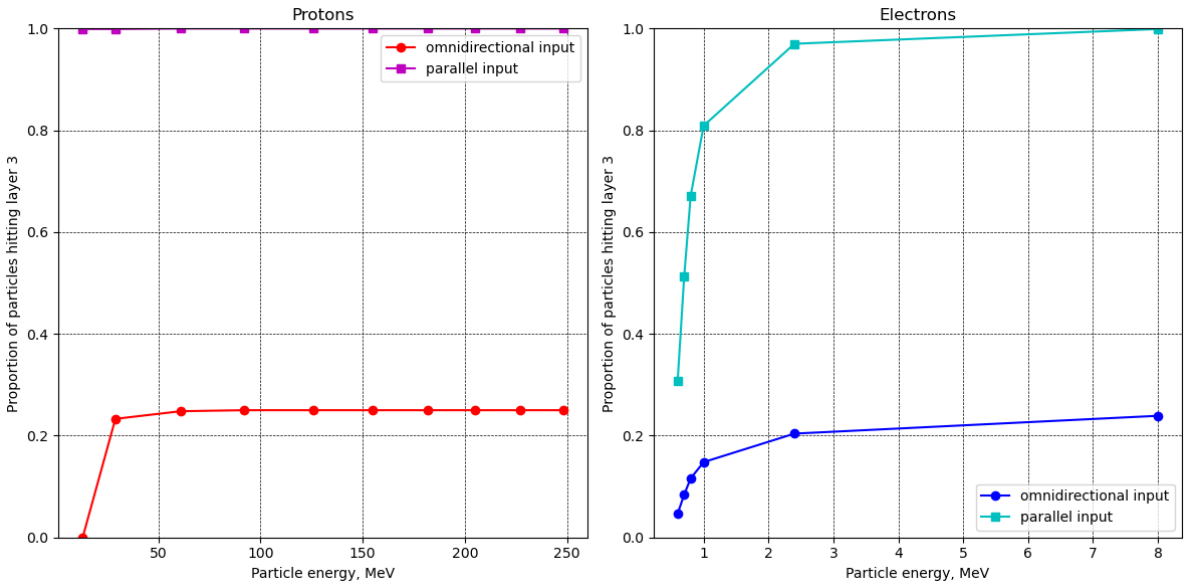

Figure 3.6: Particle energy plotted against the proportion of particles with that energy which pass through the simulated shielding. The data points are the virtual channels used in EPT for both protons (left) and electrons (right).

In Figure 3.6 for each of protons and electrons, a simulation is made using the MULASSIS tool on SPENVIS[6] of a beam of 10 000 particles, either distributed isotropically or aimed in parallel, against a slab of 0.5 mm aluminium, a 1 mm gap of vacuum, and a large amount of silicon, representing the detector itself. The simulated silicon is thicker than the actual detector to ensure that all the simulated particles are stopped. Particles will enter the aluminium and either be stopped, or be slowed and lose energy, before passing through the gap and stopping in the silicon. If one divides the particle flux found in the silicon by the original intensity of the beam, as done above, the fraction of particles that make it through the shielding results.

It's immediately apparent that approximately only 25% of the particles make it through the shielding from the omnidirectional beam compared to the parallel one. In fact, this is exactly true for the proportion of particles that enter the shielding layer at all (not shown here); for the parallel beam it is always 100% of them, and always 25% for the omnidirectional one. The explanation for this factor of 4 is a combination of two factors: 50% of the omnidirectional beam's particles come from the hemisphere not covered by the detector (no particles can hit the sensor from behind, e.g. if the back is protected by the

[6] SPace ENVironment Information System; available at https://www.spenvis.oma.be/.

satellite), and another 25% are lost due to the geometry of having a planar sensor in an omnidirectional beam [Sullivan 1971].

In particular, the number of particles incident on the detector is given[7] by Sullivan [1971] as:

$$C = I \times \Gamma$$

Equation 4

where C is the particle count rate in particles per second (#/s), I is the particle flux in #/s/cm^2/sr, and Γ is the gathering power of the detector given its area (in cm^2 sr). Assuming an isotropic flux onto a planar detector of surface area A, with particles incident on only one side, this can be written as:

$$C = \frac{F_{in}}{4\pi}\pi A = \frac{F_{in}}{4}A$$

hence

$$\frac{C}{A} = \frac{F_{in}}{4}$$

Equation 5

where F_{in} is the beam flux, and $\frac{C}{A}$ is the resulting particle flux, both having units of #/s/cm^2. For an omnidirectional beam the flux will be distributed evenly over the full 4π solid angle, and the count rate will depend on the detector aperture.

The attenuation factors obtained from simulating an omnidirectional beam to weight the EPT data will be used, as in Equation 3 above, based on the assumption that the real particle flux which is seen by the instruments is an isotropic flux. There are cases where anisotropies exist; mostly in relation to protons and heavier ions, but potentially also for electrons. The potential error can be characterised if the flux is anisotropic to some degree by comparing the parallel and omnidirectional beam attenuation factors: in the case of the strongest possible anisotropy, the weights to be used will be no higher than those obtained for the parallel beam.

3.4.2 Equating units

After the impact of shielding, a second factor is that the instruments are each mounted on opposite sides of the PROBA-V satellite. They will see the particles at the same time with

[7] if there is no back-scattering, particle loss, or particles being stopped when traversing the environment

the same phase angle (that is, the angle relative to the magnetic field), but having opposite azimuth (i.e. the particles are travelling in opposite directions). At least in the case of electrons, which are not subject to East-West or other azimuthal effects, the fluxes seen by each instrument should be identical, so a potential discrepancy in electron fluxes is discounted due to this.

Then it comes to the data itself, and the recorded values. As mentioned above, EPT records an energy flux because due to the construction of its detector assembly, incident particles will be stopped and their full energy can be reconstructed.[8] SATRAM does not, because most particles will not stop in its small detector volume. It does record a radiation dose, but that is only based on the part of particle energy deposited in the detector, not the whole energy, so that dose can't be converted to an energy flux to compare to EPT. The important point here is that for the two instruments, the quantity that can actually be directly compared between them is the particle flux. This is what will be used in the following sections.

Additionally, for both EPT and SATRAM the particle fluxes are not integral: EPT classifies its particles into multiple energy bands, giving particle fluxes in units dependent on energy (in MeV), while SATRAM distinguishes high- and low-energy particles. These energy bands can't be compared directly either, however, because SATRAM only makes that distinction based on the shape of traces left by particles, not on their deposited energy[9]. Since it's not clear what energy limits are attributed to the low channel and the high one for each particle type, they are not truly differential energy channels, and it is impossible to determine which channels should be compared between EPT and SATRAM. As a result only integral particle fluxes will be used and compared. As SATRAM is described with a shielding of 0.5 mm of aluminium which stops electrons below 0.5 MeV and protons below 9 MeV, it is a good proxy to take into account the whole energy range covered by EPT for both particle types.

To obtain a particle flux from EPT, it's only necessary to integrate the differential energy fluxes; the procedure multiplies the differential flux in each channel by the channel's width

[8] Particles must enter the telescope within a small incident angle to be recorded, which ensures that when they do, they are pointed through all of the detectors. Particles which do transit through the entire detector are not considered, because data above the energy limit of the last virtual channel is discarded for each particle type.

[9] As noted earlier, SATRAM *does* classify particle types using the deposited energy, but this information isn't given in the channels, only "high" and "low".

in MeV (Equation 2), so the dependence on MeV disappears and a particle flux results. It was also scaled by the shielding factor derived in the prior section. The SATRAM data is already an integral particle flux in the sense that its two channels are not differentiated by energy (they don't have units dependent on MeV), so it's sufficient for each particle type to sum its two channels together. The difference that remains between the two in units is then a factor of per steradians: the EPT data is directional, and the SATRAM data is not.

To equate the units of the data, either EPT's particle flux can be multiplied by the entire area of sky (the solid angle) seen by the telescope, or SATRAM's data can be divided by the same. Because the simulations of the flux seen by EPT were based on an omnidirectional differential flux, the former is the only correct option; it is not possible to go from an integral flux on a plane surface after a shielding (which SATRAM's data is) to an omnidirectional, differential flux.

4π, the solid angle of a sphere, is used for the whole sky's solid angle, because of the expectation that the flux around the satellite is isotropic. Finally multiplying EPT's particle flux by this value leaves both data sets having units #/s/cm^2, and they can now be compared.

3.5 Methodology: visualising and comparing data

Once the format of the data was established, work could begin on comparing the products between each instrument. The best way to do this was visually by making plots of the data. Since it would be necessary to analyse and amend the raw data as it was presented to us, a set of scripts were developed which would read in the data given its original format, taking any processing steps that were necessary along the way, and then plot the measurements as desired.

To briefly note the setup here, the EPT and SATRAM data sets were both received as fixed-width text files. EPT data could be downloaded from ESA's Space Weather Service[10] but SATRAM data was obtained directly from the mission team, so at first there was only one set of that data covering two weeks at the start of January 2016. (Additionally, the data for the magnetic indices described in section 2.1.4 was obtained; this also came in the form of text files.) All of the scripts were developed using Python; in particular, the `pandas`

[10] at https://swe.ssa.esa.int/web/guest/csr-ept-federated; login required

library was used to read in and manipulate the data as tables, and `matplotlib` was used to generate plots of the data.

During the project, a number of updates to the data that was being analysed were done, thanks to the assistance of the EPT and SATRAM mission teams. The results in this work are based on the most up-to-date versions of each data set.

3.5.1 Flux-time plots

The first visualisation used was just plotting the flux measurements of both instruments against time. This is simple to do and provides a quick way to evaluate the data on its face. An example of such a plot is shown in Figure 3.7.

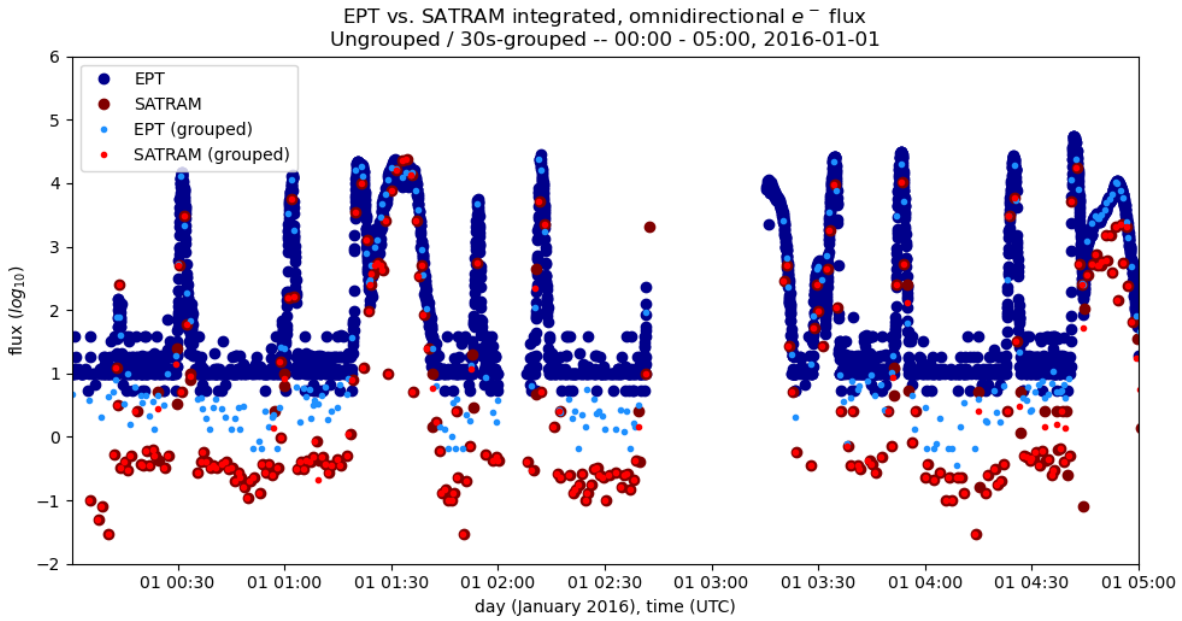

Figure 3.7: The dark blue dots represent the 2-second EPT data and the dark red dots represent the time series of the SATRAM data. The light blue and red dots represent the EPT and SATRAM data when averaged over 30 second time bins (called grouped in the labels).

As will be usual in the upcoming plots, the data is presented on a logarithmic scale of flux (with units in #/cm^2/s), since the data varies widely from hundreds of thousands of counts /s/cm^2 to less than one. The maximum for both instruments is about 10^5 counts/s/cm^2. Note that measurements where the flux was zero are removed from this view, which mainly affects the EPT data due to its high sampling cadence (compared to SATRAM).

Using this type of plot, with the very first data set received for SATRAM a large discrepancy between SATRAM and EPT measurements was observed. This appeared only

with the initial data set which was analysed close to the start of the project, but disappeared for the more up-to-date products. Nevertheless this prompted us to develop the methods mentioned in section **Error! Reference source not found.**, which were used to verify the latest data that is available.

In Figure 3.7, both EPT and SATRAM data are shown as "grouped" or not. This is just binning the data with a 30-second interval, the reason for which is explained in section 3.5.2 below. It can be seen that the data points are not affected in time by the grouping. The EPT data is uniformly lower after averaging, since high data points are very often averaged with zeroes, whereas the SATRAM data is broadly the same flux before and after grouping, since most groups have only one or no SATRAM measurements within the 30-second interval. This is sufficient to show that the "grouping" process does not affect the data in unexpected ways.

3.5.2 Flux-flux plots

To more directly compare the particle flux levels measured by the two instruments, another tool was to plot them against each other. Such a flux-flux plot should consist of points aligned diagonally along the line with a slope of unity, starting at the origin; that would represent the flux measured by each instrument rising in direct proportion with the other. If there is any deviation from this, it can be seen and characterised.

Before making such a plot, it was necessary to ensure that each measurement from one instrument is associated with a corresponding measurement from the other. As they are not taking measurements simultaneously, or even integrating for the same length of time, a good approach is just to find the fluxes from each instrument that are measured closest in time. If the measurements are too far apart, they cannot be compared, because they correspond to the satellite being in different positions with different flux intensities. A maximum time span between two data points of 30 seconds was judged to be reasonable.

To achieve the association, each dataset was grouped into bins that are 30s wide; any time bins where no measurements were captured in either data set were removed from both data sets; and the flux data of each bin was normalised by dividing by the number of measurements in that bin. Then on the flux-flux plot, each point represents one of these bins: its x-position corresponds to the flux measured by EPT in that 30-second interval, and its y-position to the flux measured by SATRAM in that interval. It is expected that the points

will be grouped roughly along the unity line, as this would represent each point showing about the same flux measured by each instrument. So the data here is presented as "30S-grouped", and an example can be seen in Figure 3.8.

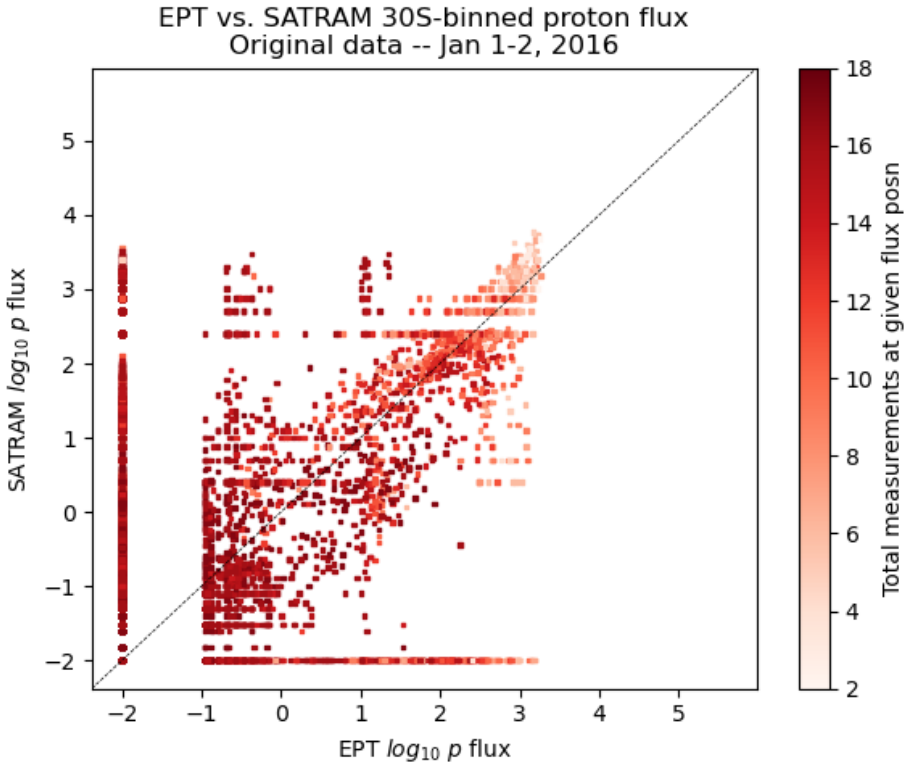

Figure 3.8: SATRAM vs. EPT proton flux data, log scale.

This displays the 30s-binned proton data from EPT and SATRAM. Each individual point represents one bin - that is, one of the 30-second periods of time making up the whole dataset - and the points are coloured by how many measurements they contain. Most of the measurements in any given bin are due to EPT - for a given time bin of 30 seconds the EPT data set has 15 measurements, while the SATRAM data set has only 1-3 measurements. As previously said, the data is presented on a logarithmic scale. Here the large number of zero-flux measurements are retained, but they are artificially set to equal -2 on the log scale, simply to keep them apart from the rest of the data. None of the data points actually reach a flux of 10^{-2}. One day worth of data is plotted here.

The general form of the proton data is evident here; it is broadly spread across the whole flux range in both directions, which represents times where flux was high as measured by EPT but low for SATRAM, and vice-versa. This can be expected due to the stronger azimuthal dependence of proton flux; such flux is highest in the boundaries of the SAA, where the azimuthal effect is most pronounced. Also in the centre of the SAA, the very

strong radiation causes may measurements to be filtered out and discarded by EPT, which similarly contributes to slightly differing fluxes being measured between instruments. There's also horizontal banding visible in the data, which appears for electrons as well (see Figure 3.11). This is essentially due to a lack of resolution in SATRAM as particles straddle a boundary between low- and high-flux regimes. When the flux sampled by SATRAM becomes too high for a given acquisition time, it is decreased so that exposures occur more quickly. There are three possible acquisition, or integration, times (0.002, 0.2, and 20 s) and correspondingly three areas of banding appear, at around 0.1, 10, and 1000 #/s/cm^2. But then the particle flux is only just high enough to be captured with the new acquisition time, so you get individual bands at 1 count per integration, 2 counts/int., etc. Because the scale is logarithmic, the bands clump together quickly as the count rate increases.

Using this type of graph, it is possible to develop a method to find and resolve any linear discrepancy in the data, by a process of linear regression which is described fully in section 3.6.

3.5.3 Histograms

The above types of graphs are useful for checking and comparing the proportionality of the data, but to analyse their capacity to represent space weather events and flux trends in space, something more detailed was needed. For this purpose histograms, displaying the particle flux seen by an instrument across both time and through the McIlwain L-parameter, are used. This is the tool which was used to derive much of the results from the given datasets, which are presented in section 4.2, but here it is explained briefly how these histograms are made.

Figure 3.9 displays such a histogram, in the configuration which was settled on to use throughout this work. There are four panels shown: the top two are histograms displaying the same interval of time and the same physical location, but different data. Figure 3.9 compares the electron data gathered by EPT from a geomagnetic storm event in 2015, to the electron data gathered by SATRAM at the same time. Alternatively the electron/proton data gathered by one of the instruments, or the data for protons across both instruments, can be shown.

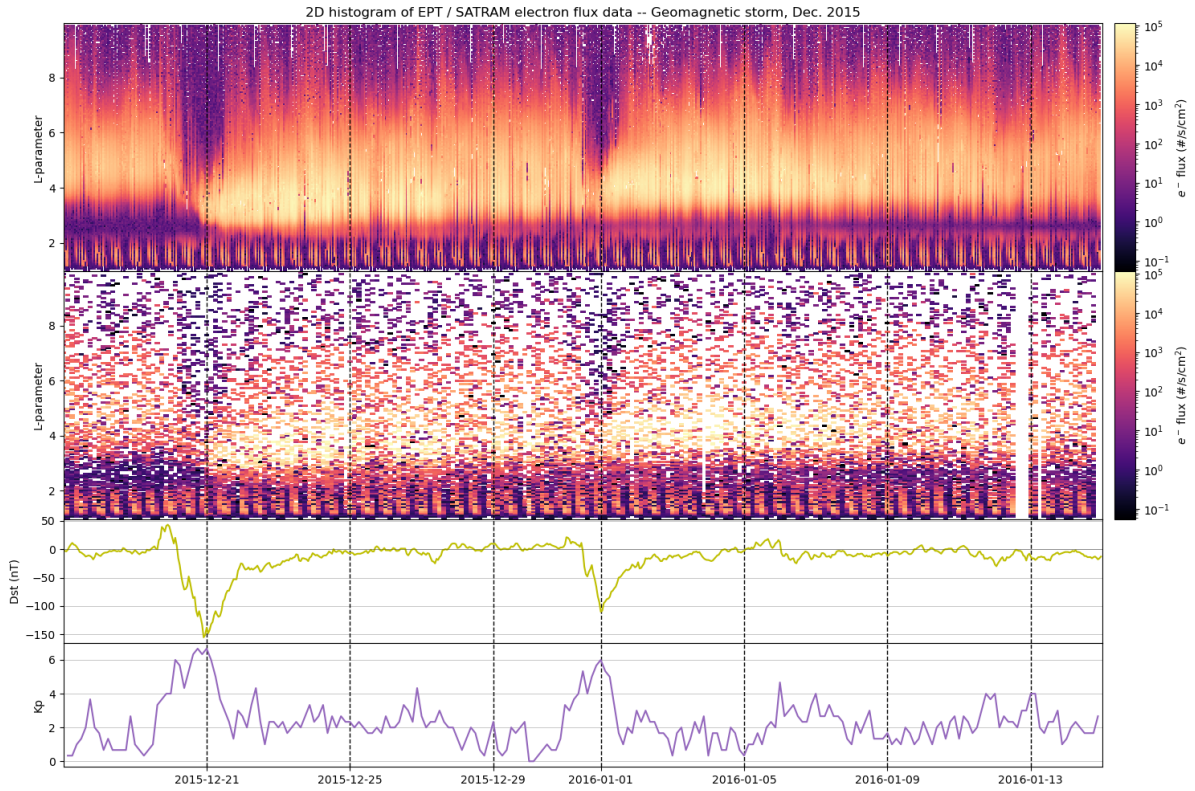

Figure 3.9, First panel: EPT flux as a function of time (in 1-hour bins) and L parameter (bin size = 0.06). Second panel: same for SATRAM flux but with bin size in in time = 3 hours and in L = 0.36. The third and fourth panel show the evolution in time of the Dst and the Kp index respectively.

In the histograms the McIlwain L-parameter (see section 2.1.5) is plotted on the Y-axis. Since only EPT actually records this parameter, it must be inserted into the (more sparse) SATRAM data, but this isn't a problem since the L-parameter depends only on the physical position of the satellite. The advantage of using the L-parameter as opposed to something like altitude directly is that it scales the data to the magnetic field, which is appropriate since the shape of the space weather environment is largely governed by that field, not to mention the field's tilt with respect to the Earth's rotation. The inner (up to $L < 2.5$) and outer ($L > 3$) radiation belts and the slot region between them are all clearly visible with this plot. More importantly, the change in the sizes and locations of the radiation belts with space weather conditions is well-visualised using this setup. Note here that the binning of the histogram for SATRAM is larger than for EPT (specifically it is three times larger in time and six times larger in L); this was necessary due to the fact that SATRAM has data that is more sparse in time.

The lower two panels are separate records of the magnetic indices Dst and Kp, shown for the same time period as in the top two panels, and on appropriate scales for each. These

provide additional information about the disruptions in the magnetic field that were recorded at the same time then the particle flux measured by EPT or SATRAM, assisting us in drawing conclusions from the data. The data for these indices is obtained directly from the GFZ German Research Centre for Geosciences. [Matzka *et al*. 2021]

These histogram plots form the basis of the primary investigations of the data, which is presented in Chapter 4 further on.

3.5.4 World maps

Since both EPT and SATRAM record latitude and longitude data, their measurements can be effectively plotted on a map of the Earth. This shows where PROBA-V was located when the measurement was taken, not relative to Earth's magnetic field, but to Earth itself. Such graphs are mostly only useful when the data is also filtered by some other criterion, then they show in which regions above the Earth that criterion holds. For example, plotting only a small section of time shows the path of the satellite over Earth at that time; plotting high-flux measurements shows where flux is high in geographical coordinates; and so on.

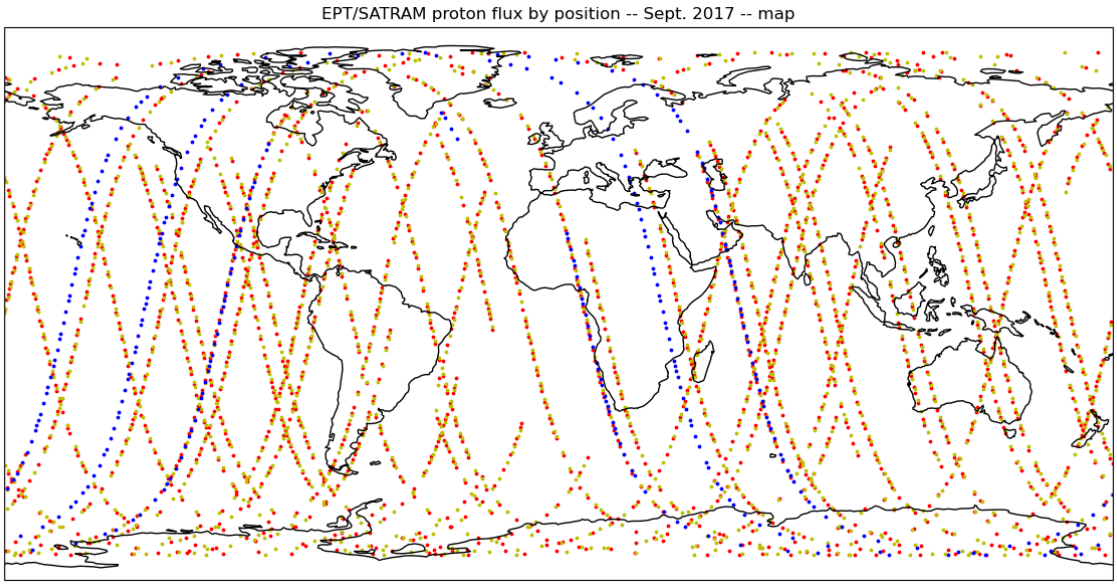

Figure 3.10: Red (EPT) and gold (SATRAM) points are proton flux measurements during the time period 10th-13th September 2017. Blue is EPT proton measurements from ten days prior, for time comparison.

3.6 Methodology: linear regression

As mentioned above, creating and examining the flux-flux plots prompted the development of some more quantitative methods to try and examine the difference in flux measurements between the two datasets. The basis for doing this is that the EPT and

SATRAM flux data are expected to be essentially the same, since they were sampling the same radiation environment at the same time. Precisely, this is known as *intercalibration*, wherein both instruments have the same response to the same flux. If the flux-flux plot slope is not unity, this either means that the instruments were not in fact seeing the same flux, or that they were not having the correct response to it. If however the data is intercalibrated, then when it is plotted on a flux-flux graph as in Figure 3.8: SATRAM vs. EPT proton flux data, log scale., it would be uniformly distributed on and around the line with slope unity, starting from the origin. This would then mean that the response from each instrument is increasing in direct proportion to the other, and in proportion to the particle flux increasing in the radiation environment.

When actually looking at the data on the flux-flux plots, it can be observed that it was actually not well intercalibrated (to varying degrees, depending on the data used). Figure 3.11 below shows an example of this. The reasons why this could happen are discussed later in section 4.1. However, already one fact is assumed: that the divergence of the data from the unity line is always uniform. This is the case in Figure 3.11, where the EPT flux is a bit higher than the SATRAM flux (or equivalently, the SATRAM flux is a bit lower), and it was also the case for all sets and subsets that were analysed. By "uniform", it is meant that the amount by which data points diverge from the unity line does not change at all as the flux changes: the data appears to be multiplied by a constant factor. In log scale, this signifies that the line is shifted by a constant amount and that its slope is unity.

The slope of the line that relates the two data sets can be found simply using the equation of a line, like so:

$$\mathrm{SATRAM} = A \times \mathrm{EPT} + B \rightarrow \mathrm{EPT} = \left(\frac{\mathrm{SATRAM}}{A}\right) - B$$

Equation 6

The aim is to determine suitable constants A, the slope of the line, and B, the y-intercept, for all values of EPT and SATRAM. This can be done by fitting models of lines to the data and taking the one which fits most closely. Actually doing this was just a matter of using the linear regression function included in the `scikit-learn` library for Python, which uses a least-squares method to fit a model to the data. A is the multiplicative constant which is sought. B could be used as an offset at the zero-flux point, to compare noise between the two telescopes, but taking into account the spread of the data and

resulting uncertainty on the parameters, it was not calculated in the present work. Moreover, the preliminary analysis did show that it is very close to zero.

Figure 3.11 compares a portion of SATRAM vs EPT data (one day in January 2016) before and after adjusting it. The raw data is shown on the left; the appropriate multiplicative factor is found by the process just described, then the raw SATRAM data is divided by that factor to yield the adjusted data, shown on the right. The exact factor is noted on the Y-axis. While a reduced portion of the data is used here to better illustrate the difference between raw and adjusted data, the results on this point from the full and latest data are described in Chapter 4.

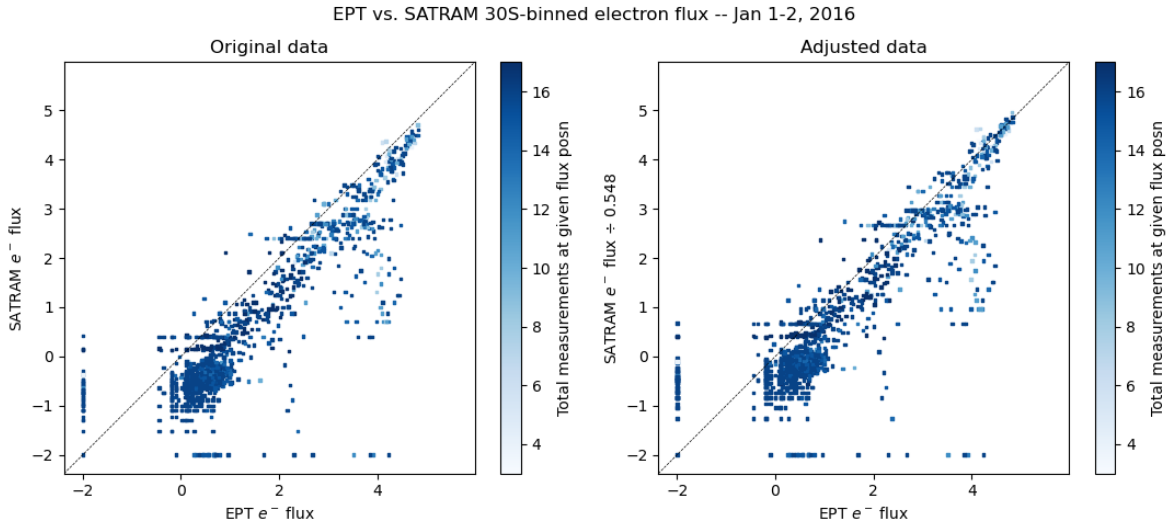

Figure 3.11. Left: data before being adjusted by the multiplicative constant. Right: afterwards. The axes are in $\log_{10}$ scale; one day of data is displayed.

4 Results and discussion

Having advanced the validation and checks performed on the datasets to ensure that the two instruments could be usefully compared, and the methods subsequently used to examine the data, here the results obtained from those methods are presented. First the intercalibration and commonalities of the data are discussed, with particularities which could be both identified and corrected; this understanding is then used to analyse a couple of space weather events from EPT and SATRAM data.

4.1 Comparison and normalisation of the data

A detailed examination of the data as gathered by SATRAM and EPT for the same time periods was then undertaken, to determine if they were properly comparable and could produce scientifically useful results when used in conjunction. The methods used for this are covered in the previous sections 3.4.2, where it was ensured that the data obtained from the two instruments was directly comparable, and 3.6, covering the method used to quantitatively check them. The following figures show the result of this comparison for the latest EPT and SATRAM data, which covers two time periods: 17 December 2015 to 19 January 2016 in Figure 4.1, and 2-30 September 2017.

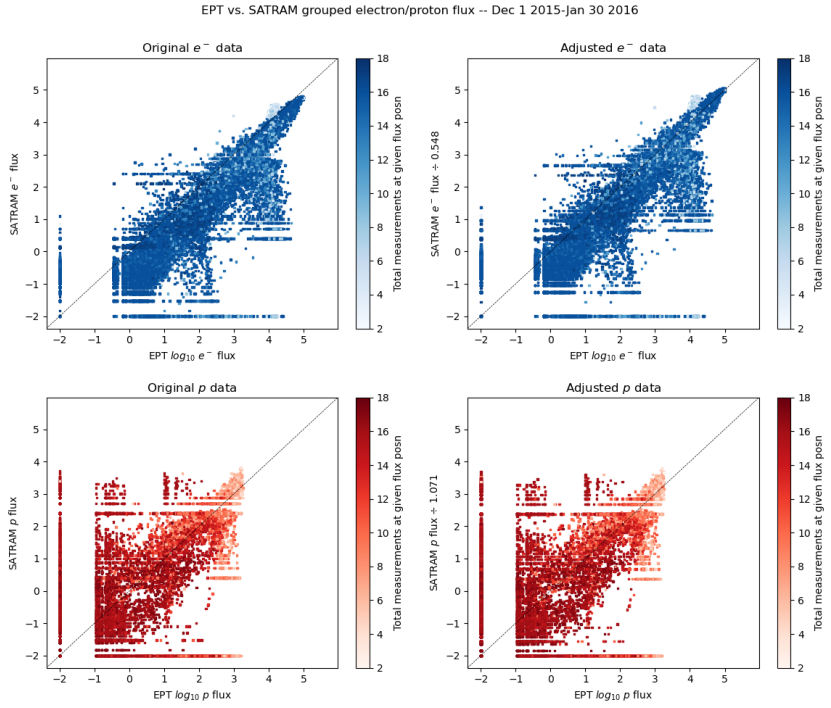

Figure 4.1: Data before (left) and after (right) adjusting with the multiplication factor, for electrons (top, in blue) and protons (bottom, in red). Data from December 2015-January 2016.

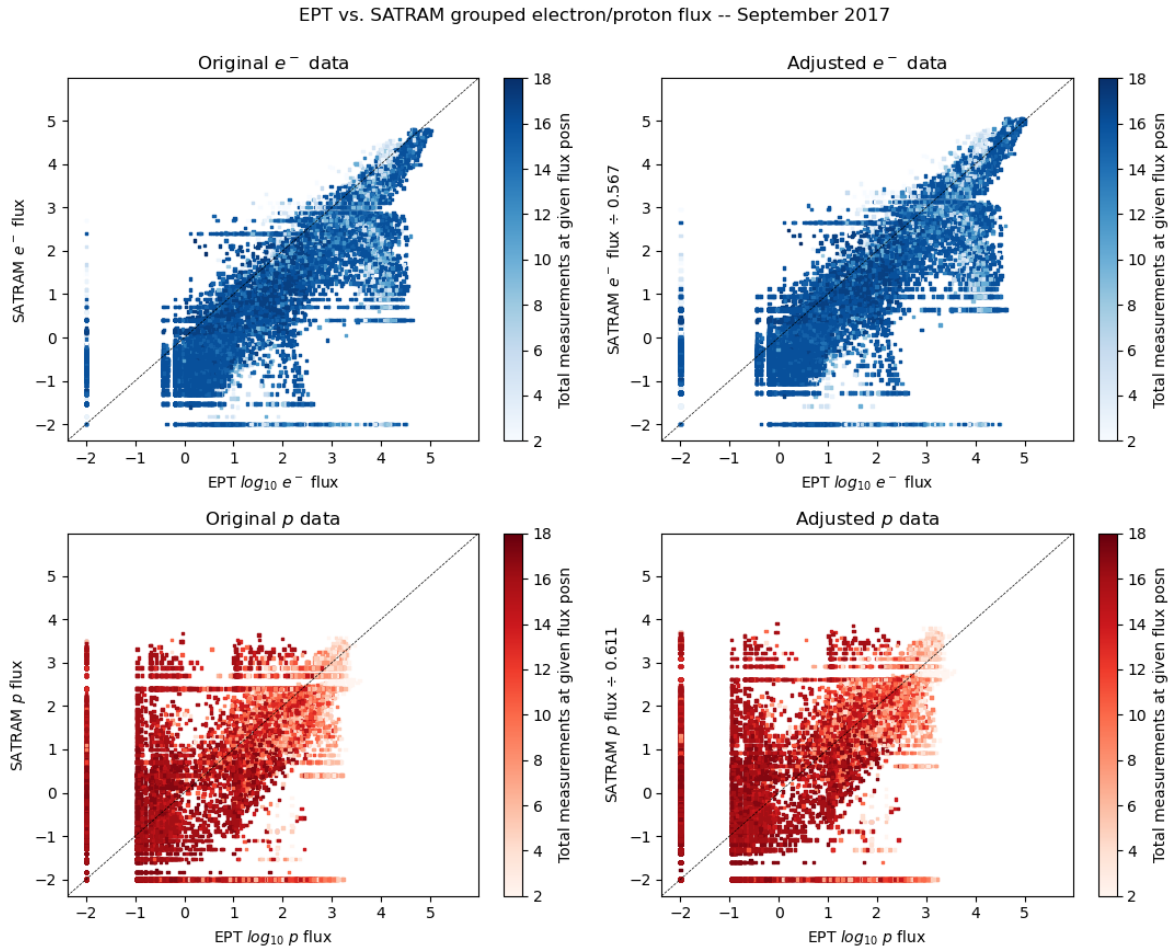

Figure 4.2: same format as 4.1, for data from September 2017

4.1.1 Normalisation factor

The multiplication factors ("A" in Equation 6) found are to be the following:

A	*2016/6*	*2017*
electrons	0.548	0.567
protons	1.047	0.611

Table 4.1: multiplication / normalisation factor A, otherwise seen as the slope of the line which the data lies on.

The fits which produced these factors have the following coefficients of determination:

R^2	*2016/6*	*2017*
electrons	0.822	0.332
protons	0.852	0.222

Table 4.2: R^2 values corresponding to each of the normalisation factors in Table 4.1.

The factor obtained for electron data is quite consistent, and reflects the consistent structure of the data. A factor of close to 2 between the data sets is definite, and was

identified rather precisely. Table 4.2 displays the coefficients of determination (or "R^2 values") for the linear fits which produced the factors in Table 4.1. A value of 1.0 indicates a perfect fit, and while values of 0.8 indicate a not-insignificant spread in the data, these are consistently good values given the shape of the electron data sets as seen in Figure 4.1 and Figure 4.2.

The factor obtained for proton data differs quite a bit between data sets here, being nearly 1 for the data from 2015-16 and closer to 2 for the data from 2017. In general, throughout the study performed during this work it was more sensitive than the electron factor was. The belief is that this is due to the shape of the data; the linear model, after all, determines its coefficients through fitting to the plotted points. For protons, since the data is so spread out, this method is unreliable where the divergence from the unity line is itself small, and consequently the uncertainty on the multiplication factor is very large. Indeed for the 2017 data, the upper-right tip of the proton distribution actually appears to move away from the unity line after being adjusted, rather than towards it. This implies that the fitting of the line is dominated by the widely-spread data lower on the graph. The low and inconsistent R^2 values of 0.332 and 0.222 support this, indicating a fit that does not intersect much of the data and hence a wide spread about the line.

The most likely reason for the SATRAM and EPT data not to be intercalibrated is either that there are some uncertainties in the processing of the raw data from the instruments. Two such contributors from processing that can be noted are the approximation of the geometry during simulation (MULASSIS simulation is done on a flat infinite layer, however the SATRAM chip is of finite dimensions with surrounding parts, and the 0.5 mm shielding is only local) or border effects on the Timepix chip (the efficiency of the chip is unknown at its edges, and particle traces may be clipped and misidentified, implying that the effective area does not correspond exactly to the geometrical area of the sensor).

But it is also possible that some physical effect does contribute to the non-intercalibration, and is not accounted for. Firstly, what is the evidence for the cause not being an environmental factor? As noted in section 3.6, the deviation of the data from the unity line is always uniform; it does not change at all with changes in the flux, nor over time. This would be unusual for some real, physical phenomenon that was affecting the fluxes as seen by EPT and SATRAM. For example, SATRAM is prone to picking up other particles such as cosmic rays and gamma rays, due to the nature of its detector; though they don't deposit

much energy, they leave a trace similar to electrons. These would certainly be random and not a constant contribution to the flux; the recording of too many extra particles in the electron channel would also have as a consequence that SATRAM fluxes would be larger than EPT fluxes, and not smaller as is the case here.

Secondly, there is the possibility that the cause is an anisotropy in the particle fluxes. EPT and SATRAM do view the same radiation field at the same time, but from opposite sides of the satellite onto which they are mounted. If the radiation field varied in flux with direction, the two instruments would see diametrically-opposed fluxes, which could explain the uniform discrepancy between the data sets. For electrons, this is not expected to be the case; electrons are known to be more or less isotropically distributed in the radiation belts - their flux has a low dependence on their pitch angle relative to the magnetic field. So a non-isotropic radiation field seems unlikely for electrons, and this is therefore discarded as an explanation.

Protons, on the other hand, are known to show a steep pitch angle distribution in the inner belt, and are subjected to east-west asymmetry when at the border of the South Atlantic Anomaly (recall that this is where the border of the inner radiation belt intersects with low earth orbit). While the pitch angle is the same for EPT and SATRAM, the azimuth direction is opposite due to the mounting. An azimuthal anisotropy therefore could contribute to the spread of the proton data, although this latter may primarily be attributed to the low count of protons and corresponding low statistics.

Thirdly, how can we tell which instrument is actually causing the deviation, or if it isn't both of them? Though it appears in figure 3.9 that the SATRAM data has lower flux than the EPT data and pulls it below the unity line, that's also what would appear if SATRAM was accurate and EPT was artificially higher. To decide which instrument is responsible for the error, some external information must be used. While presently there does not exist any information on cross-calibration for SATRAM, EPT proton data at least has been compared to datasets from other particle telescopes. These are on different satellites, but in conditions where - due to physical processes - the measured fluxes are expected to be the same - e.g. at high latitude during SEP events or in the SAA at a same position [Borisov et al. 2014]. An example is a comparison with GOES shown in Figure 4.3: A flux-flux plot of proton data from EPT versus data from the GOES satellite; see also the instrument calibration done in Cyamukungu et al [2014]. Based on this condition, it was decided to apply the found

calibration factors to the SATRAM data, but they could as easily be applied to the EPT data with the same results. With more calibration work, a better determination could be made in this area.

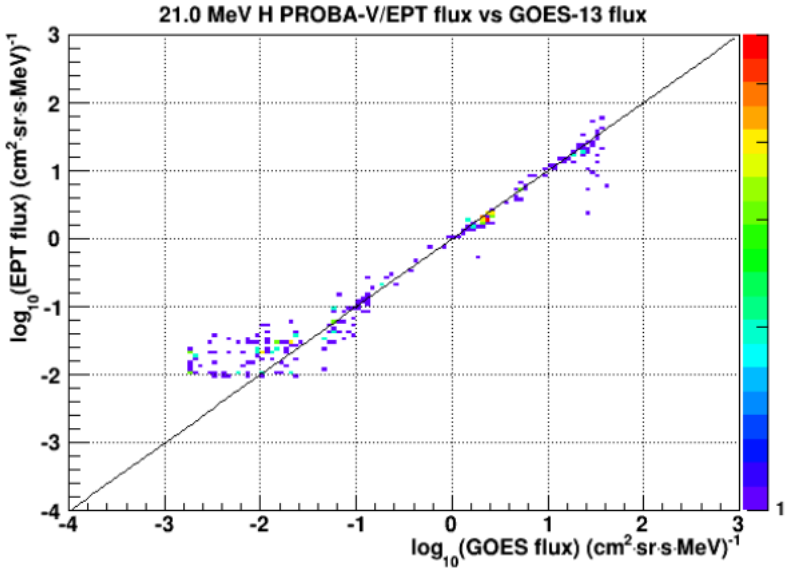

Figure 4.3: A flux-flux plot of proton data from EPT versus data from the GOES satellite, during September 2017. Adapted from Figure 11 of Borisov et al. *[2019, p. 36].*

Finally, for protons, despite the uncertainty in the obtained calibration factors there are some environmental factors which could go a ways toward explaining the discrepancy between the EPT and SATRAM data sets. Especially of note is that the correction factors obtained are quite different between the two proton data sets. In the December 2015 - January 2016 proton data set, only fluxes from the SAA are included, where the angular distribution is steep. In the Sep 2017 data set, data from a SEP (see sections 2.1.3 and 4.2.2) is additionally present, wherein the proton flux is isotropic. Although the SEP flux is only present over c. 1 week, it may have some influence, since EPT records explicitly directional data while SATRAM has the 2π FOV and direction-dependent efficiency [Granja *et al*. 2018]. The effect of this needs to be investigated. Additionally, contamination of EPT proton data was observed in the presence of high electron flux above 2 MeV (see section 4.2.2 and Figure 4.10).

4.1.2 Shape of the data

In Figure 4.1 and Figure 4.2 above, while there is the broadly uniform shape of the data and deviation from the unity line, significant non-uniform features are also apparent. Already mentioned (in section 3.5.2) are the horizontal bands which are an artefact of the

integration time used by SATRAM[11]. But much more prominent, in the electron flux data, are the "legs" which stretch down from the central band of data. Their position signifies apparently-depressed flux seen by SATRAM (or heightened flux seen by EPT). In addition there is a small "eye" feature at the top (located near x=4.2 y=4.2), most clearly seen in Figure 4.1 and indicated again in Figure 4.4, which signals the opposite.

The cause of these features can potentially be identified by finding commonalities among them, the most obvious being that each "leg" is at a completely distinct flux level (x=2 and x=4). Given what was mentioned before about the banding being caused by the interaction between SATRAM's integration time and the flux it is measuring, it also seems useful to see if that is common in each group.

For the coming graphs, the electron flux data from 2015-2016 is considered. The lower leg is defined as the points lying between 1.5 and 2.5 #/s/cm^2 of flux as measured by EPT (X-axis, in $\log_{10}$ scale), and between -1.3 and 0 #/s/cm^2 from SATRAM (Y-axis, also $\log_{10}$ scale). The upper leg is bounded by 3.5 and 4.5 on X, and 1 and 2.1 on Y. The "eye" is bounded by 3.95 and 4.28 on X, and 4.18 and 4.6 on Y. Figure 4.4 highlights these features; because of their shape, this graph was nicknamed the "lizard".

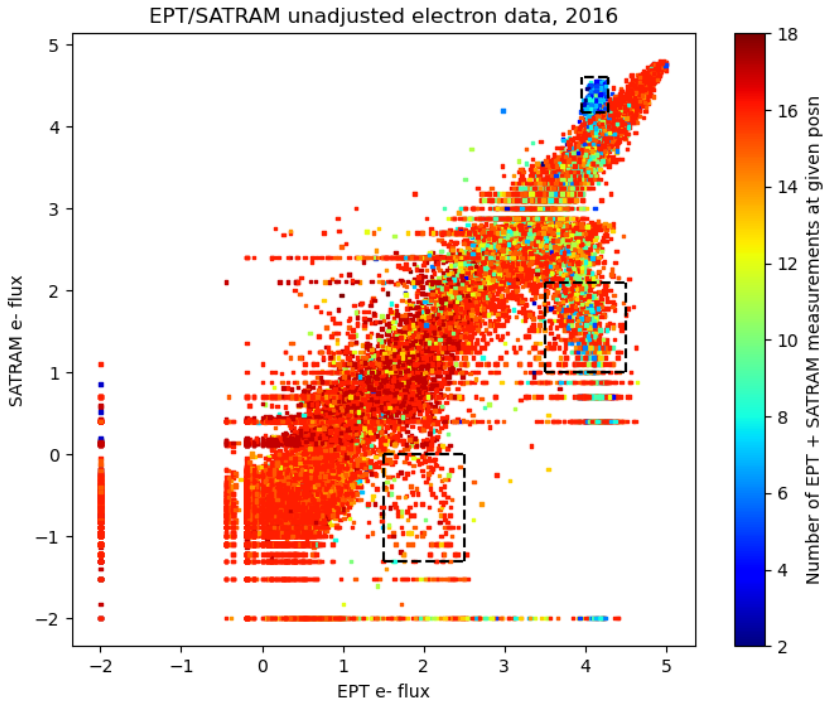

Figure 4.4: the lizard. Flux values are in $\log_{10}$ scale (1 = 10^1 counts/s/cm^2, etc.).

[11] they also appear on the EPT data, but to a lesser extent, as they are only visible at low fluxes.

The previous graphs have shown points coloured by the number of measurements at that flux position. Because the points are just placed as in a scatter plot - one point for each 30-second bin, at the average flux in that time-bin - they overlap heavily. To get a clearer picture, the plot is modified slightly here to display them as an actual histogram - see Figure 4.5. On the z-scale, the occurrence of data within one SATRAM-EPT flux bin is shown. The bins are 0.05 wide in both X and Y directions, in the log10 scale.

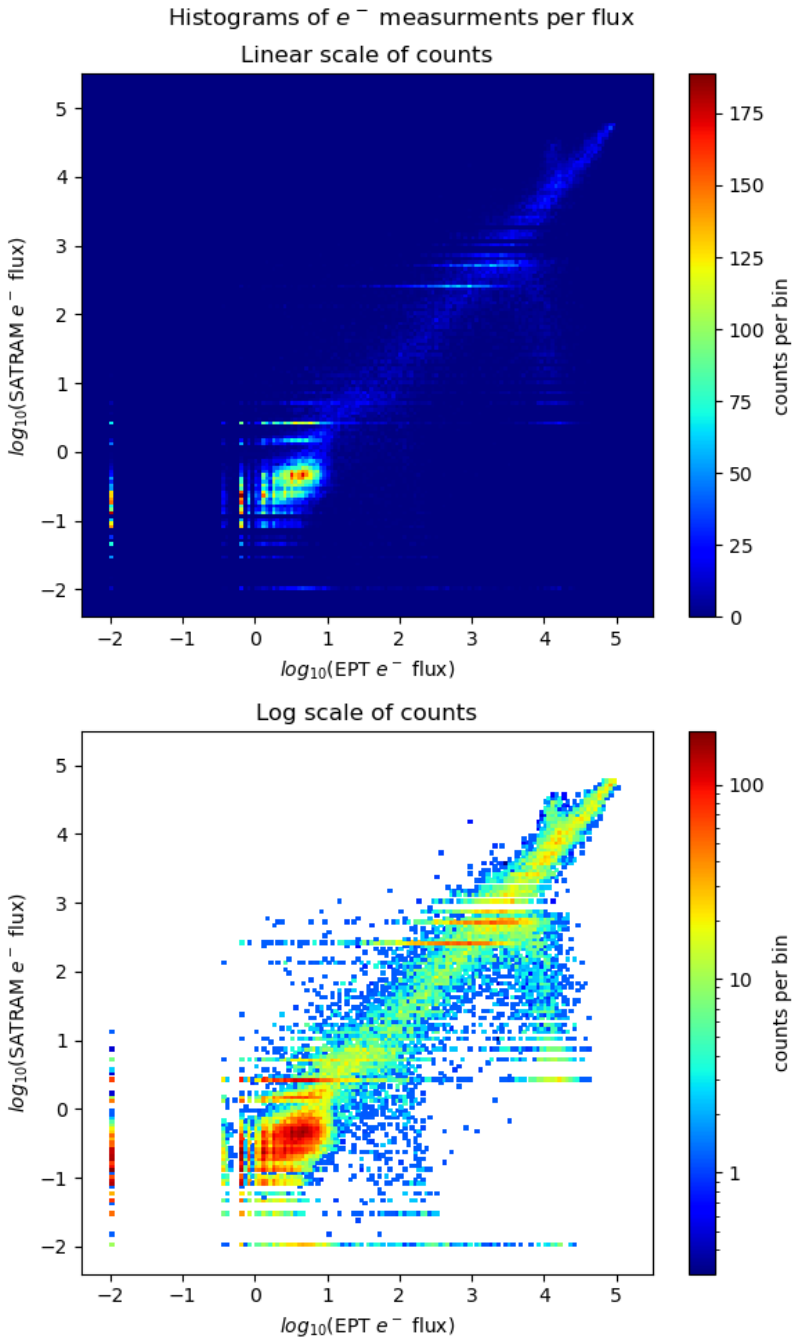

Figure 4.5: 3D histogram of the SATRAM-EPT flux distribution. The Z-scale shows the number of counts in one bin. Top is in linear z-scale, bottom in log z-scale (where white bins are empty). Bins are 0.05 flux units wide.

From this figure it can be seen that the vast majority of counts in the entire data set are taken at times of low flux, or even no flux. If one compares the path of the PROBA-V satellite to the locations of highest flux (the radiation belts and the SAA), the satellite spends most of its orbit outside of them, and so most measurements would be expected to record low flux. The "legs" are actually quite sparse structures[12], compared to the bins that make up the central lines, which are relatively full. The "eye" is in Figure 4.5 comparable in colour to the rest of the central line, so it seems to be caused by a different phenomenon than the legs.

Next, the data is grouped by SATRAM's integration time (or acquisition time, as it is labelled in the data). As was stated before, this is the time between the beginning and end of one exposure of the sensor on the Timepix chip, and it is either 0.002 seconds, 0.2 seconds, or 20 seconds, depending on the flux that the chip is recording. The time before a new exposure actually begins is variable and not predictable. Figure 4.6 shows the same data filtered for all three possible integration times.

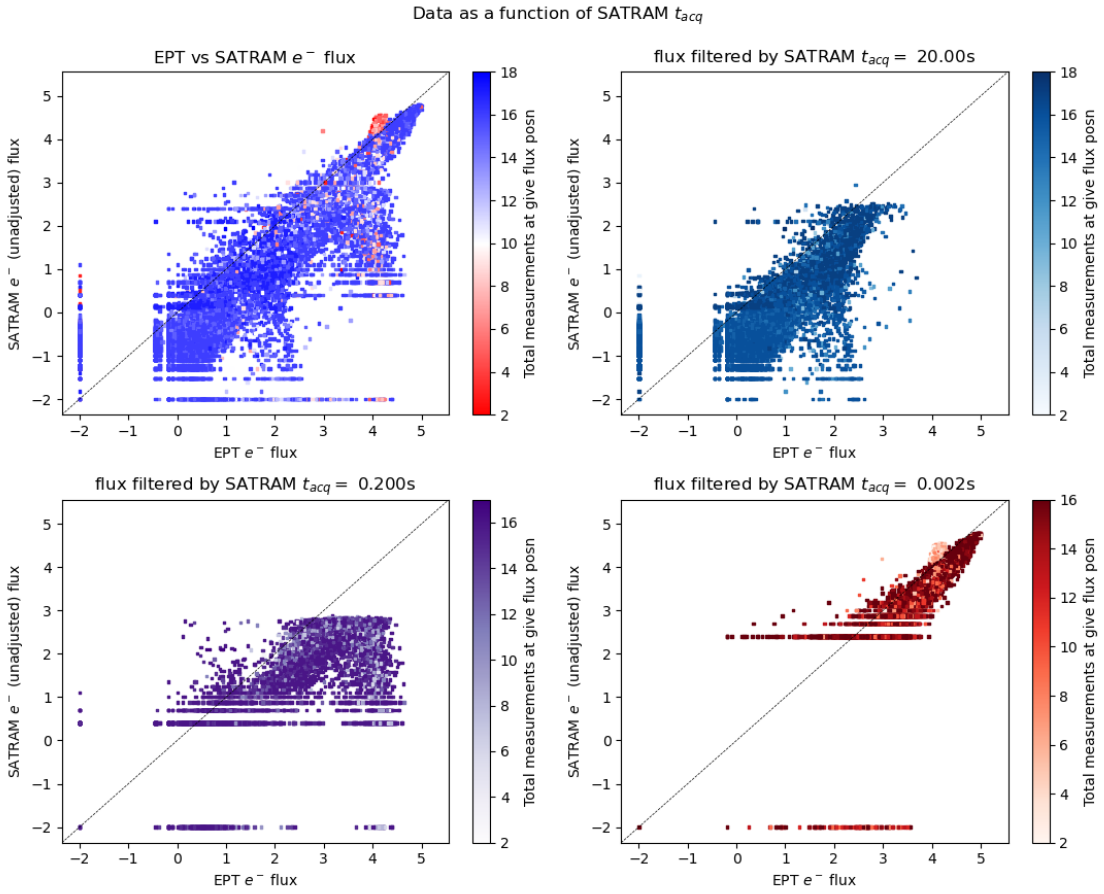

Figure 4.6: a) all data, b) data that had an acquisition time of 20s, c) time of 0.2s; d) time of 0.002s.

[12] when evaluated numerically, ~20% and 10% of the data is in the upper and lower legs, respectively

Again, the link between SATRAM integration time, flux, and the horizontal banding can be seen in this figure. The bands begin only when the integration time is shortened, and they correspond to lines of integer counts (#/sec/cm^2). The bottom leg only exists in the 20-second regime, the upper leg in the 0.2s regime, and no measurements from either structure appear in the 0.002s regime. As a side note, the zero-flux measurements (recall these are set to a value of 10^{-2} on the log flux-flux graph) also appear in every integration regime. They are much less common for SATRAM (for which they lie on the Y-axis) at higher integration times because it is much less likely to have a blank CCD when it does read out. Conversely EPT always records a measurement every 2 seconds, so it captures less data with zero flux when the average flux is high and more data with zero flux when the average flux is low.

A last thing that can be examined is which spatial regions the data that makes up these features was collected in. Filtering the data to only include the features, and plotting by its longitude/latitude coordinates on a map allows this to be done, as in Figure 4.7.

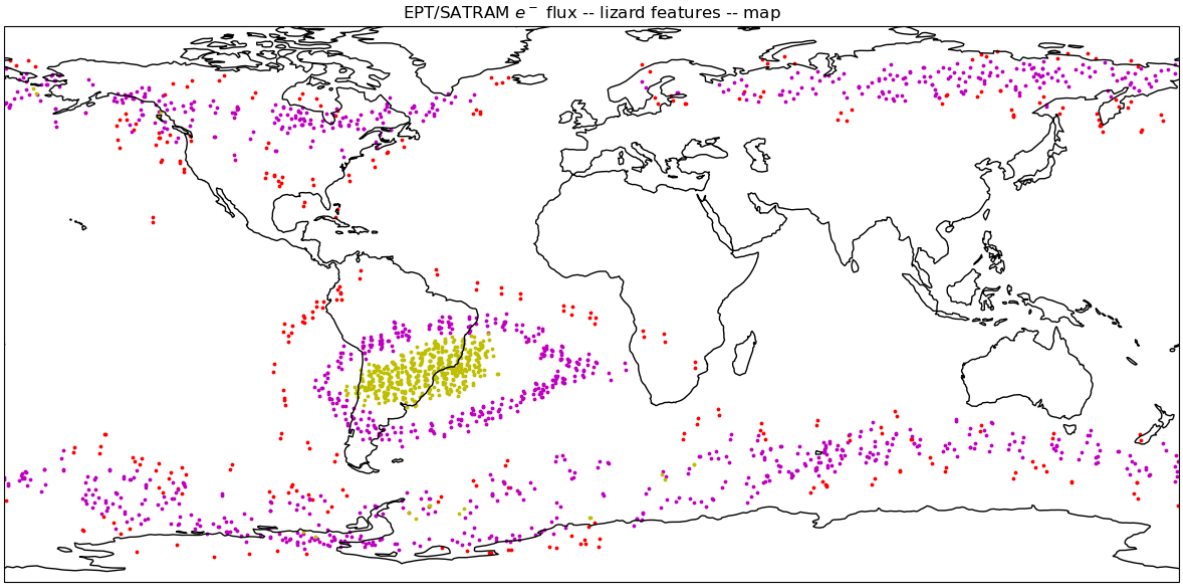

Figure 4.7: Geographical distribution of the data from the three selection areas in Figure 4.4: red points are from the lower "leg", purple points from the upper "leg", and gold from the "eye".

Looking at the data this way is consistent with the earlier observation that the features come distinctly from certain flux regions. The wavy bands traced out by the red and purple points are the radiation belts, where they come closest to touching Earth up in the polar regions. The South Atlantic Anomaly (SAA) is visible in the expected place as well. The red points, corresponding to the lower leg feature, are clearly drawn from the outer edges of

the radiation belts and the SAA; the purple points of the upper leg correspond to the inner edges which have higher flux; and the gold points of the eye are almost entirely confined to the core of the SAA where electron flux is highest. A couple of gold points do show up in the very centre of the outer radiation belts as well; there are some near Alaska and the Bering Strait. Compare Figure 4.8, a map obtained from the EPT data source of the latest weekly electron flux data at time of writing; the radiation belts and the SAA are highlighted as the regions of significantly higher particle flux.

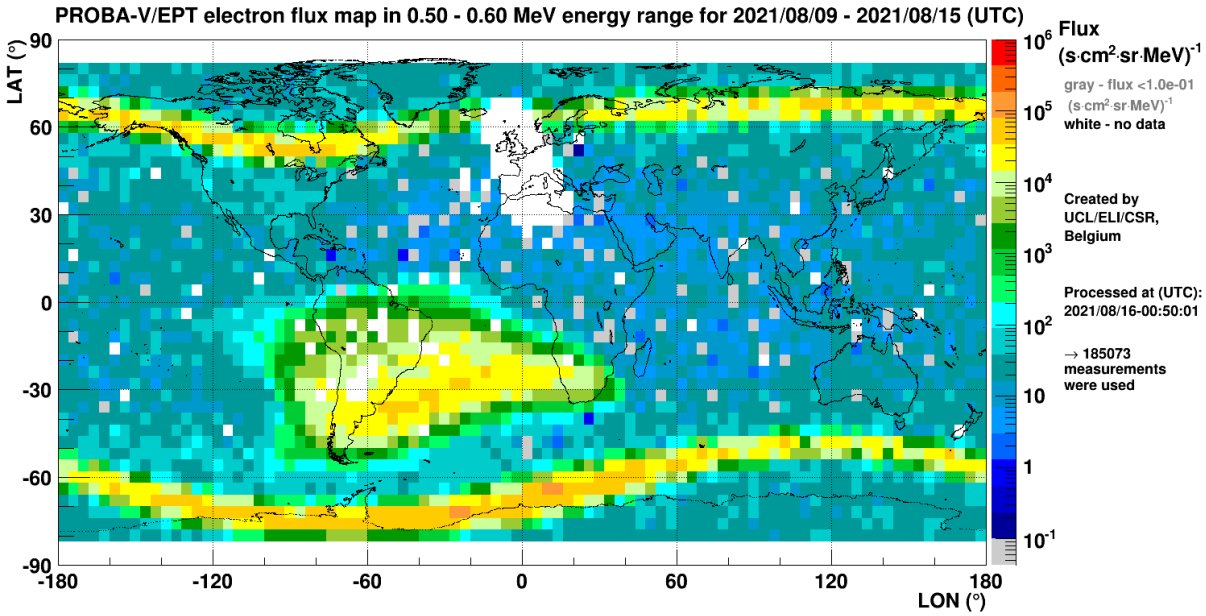

Figure 4.8: a geographical map of electron particle flux as measured by EPT.

Having therefore confined each of these three features to a) a single one of SATRAM's integration times, and b) a high-flux region within that integration time regime, it remains to answer why they appear. As mentioned just above, the legs of the lizard appear to have a separate cause to its eye - because of the differences in count frequency as seen in Figure 4.5. One speculation for the legs is that they have a similar cause to the horizontal bands, in that they are measurements taken when the SATRAM integration time is not well-adapted. Specifically, it is when the integration time is too long for the flux level being encountered, and should have been switched to the next-shortest integration time. This causes particles to heavily cover the detector, such that their traces overlap with the traces left by earlier particles in the same frame.[13] This will naturally happen at the limit between the level of flux that is suitable for one integration time and the level that's more suited for the next one, as

[13] See Figure 3.5 for a reminder of what the traces look like on the detector.

they will overlap somewhat and the instrument can only react and make the switch in reaction to being saturated like this.

The ultimate result of these overlapping traces is then that the particle classification algorithm, used by the SATRAM team to process data after having been downloaded from the satellite, tends to associate traces to the wrong particles. A speculative explanation is that the algorithm is seeing some of the overlapping traces of many high-energy light particles as just large blobs typical of single particles, or is rejecting these overcrowded areas as non-identifiable image patterns, and so miscounting the number of light particles on the frame. This would explain the low SATRAM flux as compared to EPT flux in the "leg" features. This shows that although overcrowded frames have been filtered out, some optimisation may still be applied.

The classification algorithms used by the SATRAM team are of course more sophisticated than this description suggests, as they also make use of the incidence direction and deposited energy per-trace to identify particles (see section 3.3). It would be interesting to examine other data such as the dose rate in these off-centre measurements to see if that is also affected in these particle-saturated regimes. However, it is noted in Granja *et al*. [2016] that at very high flux levels, exactly which cause "signal overlapping among particle clusters" [*Idem*, p. 120], that pixel energy detection is stopped, so that additional information isn't available. Regardless, this went beyond the scope of this work.

The lizard's eye, then, is a bit easier to explain and is apparently due to EPT. Since it is off the centre line to the left, it represents lowered EPT flux compared to the SATRAM flux. After discussion with the EPT team, our speculation was that in this region electron fluxes given by EPT are underestimated due to pile-up of electron signals, mainly with the very frequent high proton signals (especially in the S1/S3 sensor). This is also the reason why most of the data is filtered out in that region [Borisov *et al*. 2019]. At very high flux, the count rate no longer rises in direct proportion to the real flux, which means the detector isn't really "counting" particles anymore and its flux response is not reliable.

4.2 Observation of space weather events

In this chapter two types of space weather events are presented as seen simultaneously by both instruments. Features common to these types of events are identified based on the data visualised here, and the specific events are analysed.

4.2.1 Geomagnetic storms

Around the new year in 2016, two strong geomagnetic storms hit Earth and their effects were recorded by PROBA-V. Geomagnetic storms are described in section 2.1.3, and generally result from heightened solar activity which energises the magnetosphere. Figure 4.9 displays the data gathered by EPT and SATRAM in the days surrounding and following the storm. Note that for this and all following histograms, the bins are 1 hour and 0.06 L-values wide for EPT data, and 3 hours/0.36 L-values wide for SATRAM data.

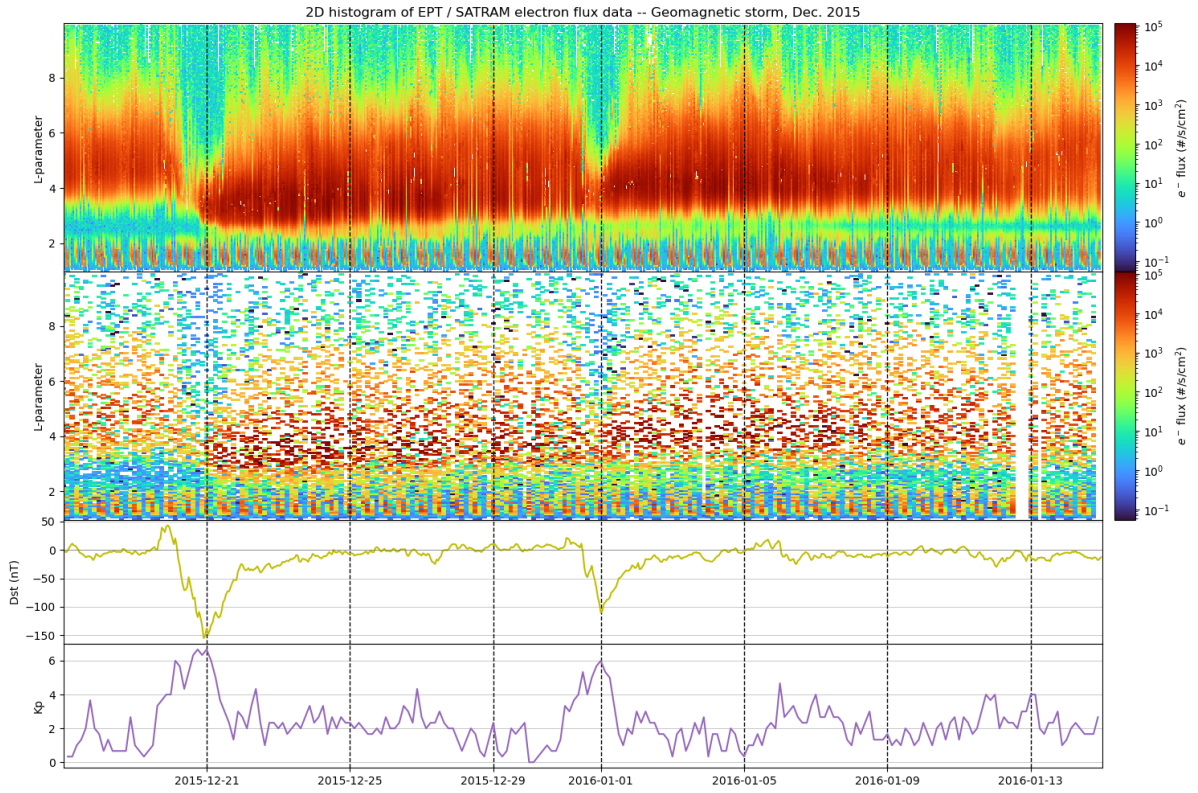

Figure 4.9: EPT (top panel) and SATRAM (2nd panel) electron flux data over time, 17 Dec 2015-14 Jan 2016.

Since geomagnetic storms don't strongly affect the proton flux in the radiation belts, Figure 4.9 focuses on the electron flux. The onset of the first storm is evident as December 20th begins, characterised by the point where the index Dst increases. Dst is a measure of the strength of the ring current (see section 2.1.4); a geomagnetic storm perturbs it and causes it to generate a B-field, which is seen as this increase. This is followed by the storm itself, seen immediately afterwards when Dst drops way down, to 150 nT below normal. This is mirrored by a sharp increase in the Kp index, and tracks a sudden decrease in electron flux seen by both EPT and SATRAM, as the outer radiation belt essentially disappears briefly. The

portion where the belt disappears (seen as a sort of break just before December 21st) is known as “particle drop-out”, since particles seem to disappear from the radiation belt.

The particle drop-out is followed by the recovery phase, as the Dst index returns to normal. At the beginning of this phase the particle flux in the outer radiation belt has returned, but the belt is strongly depressed, being pushed down to about touch the inner belt and erase the slot region between them. The flux, as the colour scale indicates, is actually more intense than it was before the storm, because of the extra particles captured from the solar wind and their increased kinetic energy gained mainly from wave-particle interaction, and to some smaller extent from reconnection.

On New Year’s Eve, the second geomagnetic storm strikes, first depressing the outer belt and then noticeably heightening the flux. However, unlike the first storm which completely filled the slot region with electrons from the outer belt, this storm only has a minor effect on the flux in that region. Over the course of the next few weeks into the middle of January, the magnetic field slowly recovers with the decrease of the ring current energy, and the slot region reappears. The “decay time” characterises how long this process takes after a given magnetic storm. In this case, it takes at least three weeks to recover, probably closer to a month for the slot region, as the inner edge of the outer belt is still as low as $L = 3$ by the end of January.

Note that the inner radiation belt does not feel the effects of a geomagnetic storm unless it is a particularly strong one [Pierrard and Lopez 2016]. Here, the effect on the inner belt was indeed minor.

Tracking the onset and effects of these storms is clearly easiest to do with EPT, due to its richer dataset. But despite SATRAM being more sparse, it is perfectly serviceable for this purpose as well. Both storms, the increase in flux and the movement of the belt can be seen solely through SATRAM’s data. Also, after having corrected with the multiplication factor mentioned above, they register the same fluxes as well - all of which is promising.

4.2.2 A solar energetic particle event

The other space weather event which was examined is a solar energetic particle event, or SEP, that took place in late 2017. SEP events are also detailed in section 2.1.3; a catalogue of known events is available at the NOAA Space Environment Services Centre [Gurman

2021], where the two latest events on the list (at time of writing) are examined here. Figure 4.10 displays the effect of the SEP on particle fluxes in the Earth's magnetic field.

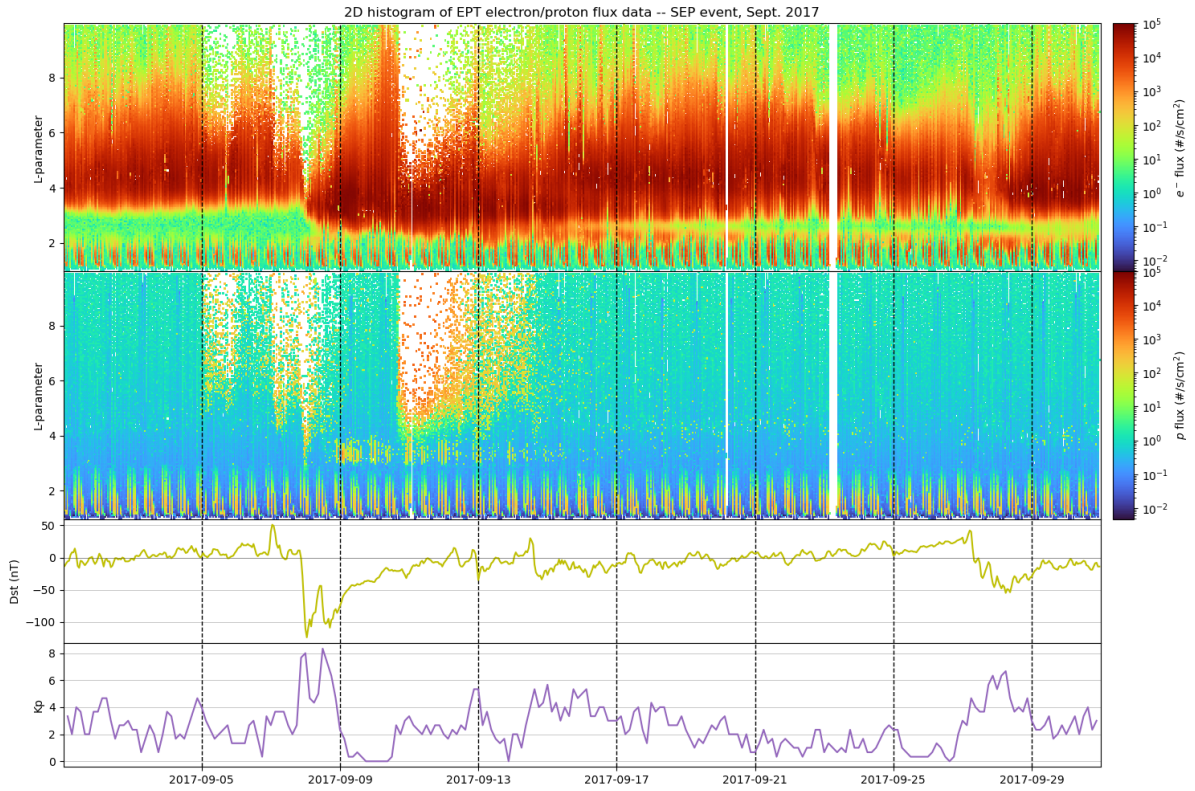

Figure 4.10: EPT electron (top) and proton (2nd panel) flux data over time, 02-30 September 2017.

In contrast to an ordinary geomagnetic storm, SEP events are notable for their effect on the proton flux. This is a direct result of the solar protons carried from the Sun and impacting Earth as part of a coronal mass ejection or an accelerated solar wind. To capture this effect, Figure 4.10 shows the electron and proton fluxes together, as measured by EPT only. The SEP appears to generate a storm event which has as strong an impact on the electron flux as the geomagnetic storm did, but it has an enormous impact on the proton flux at $L > 3$ which is evident around September 7th, and even more so on the 10th. The normally quiescent flux of protons is energised to figures of 10^2 and 10^3 counts/s/cm^2, while the outer radiation belt is heavily depressed.

Compared to the previous event, this one has a noticeable impact on the inner radiation belt, creating an additional structure in the slot region with electrons that even reaches the inner belt. This latter structure, stretching from a bit over $L = 1$ up to around $L = 3$, is shown on these histograms in the form of a striped pattern; this corresponds to the moments in time when PROBA-V is passing through part of the South Atlantic Anomaly on a given orbit (on stripes of high flux) and where it is not (stripes of low flux), as its orbit

processes around the Earth. This is because at its altitude, the SAA is the only region where the inner belt comes close enough to Earth, so that's where it is sampled by EPT and SATRAM. The outer belt is sampled at the polar regions, which PROBA-V passes through on every orbit (unlike the SAA, they cover their entire longitude range). The location of the belts is visualised in Figure 4.8 above.

We also notice that these stripes reach up above $L = 3$ to $L = 4$ in the proton histogram, retaining the stripe pattern that is particularly visible between 9 and 14 September. This is not, as it appears, protons filling the slot region. In fact, the protons between 13 and 61 MeV during that period are contaminated by an extremely strong flux of electrons above 1 MeV (EPT became vulnerable to this issue particularly after the degradation of front sensor gain in 2014 [Borisov *et al.*, 2019]). The contamination of the two proton channels in that energy range inevitably leads to contamination of the entire integral spectrum.

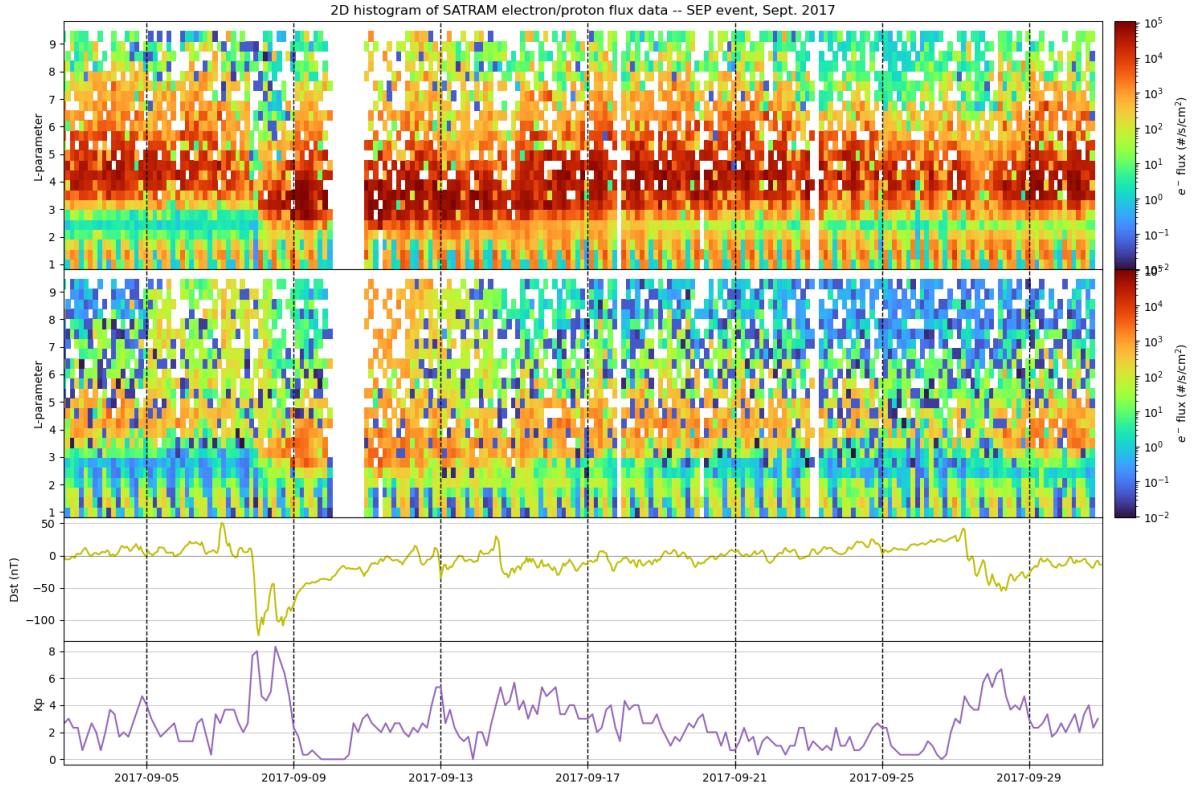

Figure 4.11: same form as Figure 4.10, but from SATRAM electron and proton flux data.

We can also examine this event through the lens of SATRAM. As usual, the data is much more sparse even after increasing the bin size a bit. But with that, we are still able to see the same features as for EPT. The proton flux is generally lower, but is strongly affected by the SEP, as the electron flux is. Flux in the outer belt is greatly increased by the event, before

decaying to normal over the course of weeks. We do not draw any new conclusions from this, but again it supports what we see with EPT.

In this set of EPT data, some gaps are also present, the largest ones at about the 20th and 23rd September. These white areas are not places where the flux was zero (those are just assigned the darkest colour on the scale), but rather places where there was no flux measurement in the bin at all. This would have occurred on the mentioned dates either due to problems with the satellite itself, or with data transmission, such that the data is not available. White portions can also be observed on the 6th, 8th and 11th-12th at $L > 4$. Here, the satellite was able to transmit, but the data was filtered out as low quality due to the intense radiation (see Borisov *et al*. [2019] for a description of EPT's filtering, if desired). This colour scheme also applies to the SATRAM histogram, where a white background also signifies the data was not transmitted, the instrument was simply not measuring, or the data was filtered out.

5 Conclusions and future work

In the course of this project, a comparison and intercalibration of the EPT and SATRAM instruments aboard the PROBA-V satellite was performed, which both have the task of detecting charged particles but with a very different construction and purpose. This involved comparing properties of each instrument's measurements, done by a thorough examination of the individual data products and properties of each instrument, and then by a detailed comparison of both data sets together. A variety of methods were developed to perform these tasks, and they allowed to achieve useful results in finding general correlation between the datasets, as well as tackling several features arising from the detection or processing techniques applied in each of these two instruments.

It was found that in general both instruments have a comparable linear response to particle flux, such that they can be used to give parallel views of space weather events and phenomena. With the latest data available, the corrections needed for SATRAM's data products to ensure the best correspondence with the EPT fluxes were estimated and applied, in the form of a simple multiplicative factor applied to the SATRAM measurements. These factors are given in Table 4.1, reproduced here:

	data from Dec 2015/ Jan 2016	*data from Sept 2017*
electron flux data	0.548	0.567
proton flux data	1.047	0.611

Despite the general linearity which holds, features were also identified in the EPT and the SATRAM flux data which deviate from the overall linear flux response. These results were forwarded to the SATRAM team to hopefully assist in improving their processing algorithms. The tools elaborated during this work can be used for future comparison and analysis of these datasets, in order to further improve their precision.

Overall, while SATRAM provides less detailed information about the radiation environment compared to EPT, not reporting differential energy fluxes and providing them at an interval roughly ten times longer, it is still a good radiation monitor with an appropriate linear response to flux. It can be used to sample and examine broadly the same types of space weather events as EPT can, and is no less than a good complement to a science-class spectrometer-type instrument.

Once having a good understanding of the instruments and their data products, in theory and in practice, and notwithstanding these corrections which remain to be made on the data, two types of space weather events were examined: geomagnetic storms and a solar energetic particle event. It was possible to identify from the data itself prominent features which are typical of each event, and to characterise them to some extent with their effects on radiation flux, the radiation belts and decay times. This serves as an example of future comparisons which can be made using EPT and SATRAM data in conjunction.

To process the data and implement the methods used to analyse and correct it, a set of Python scripts was developed which could read and manipulate data products from EPT and SATRAM. This code is publicly available on demand for use and improvements in making similar analyses between these two instruments.

Future work in this area should continue the cross-comparison of SATRAM and EPT data with the newest data products, to assure the best possible calibration for each of the instruments. One factor which was not investigated was the potential presence in SATRAM data of X-rays, due to bremsstrahlung in the detector silicon, muons and cosmic rays. Characterising the frequency of counting of such additional particles may give further accuracy to the flux data. Also, a study with an exact geometry of the SATRAM detector should improve the precision in the intercalibration process.

A further area of study which was envisaged for this project, but which was not reached due to time constraints, was to determine ways in which the data from each instrument can be used to complement the other. An example is taking advantage of the different facing directions of each instrument aboard the satellite, to examine events which have an azimuthal dependence, such as at the onset of a SEP event. During strong geomagnetic storms, the effect on proton flux could also be compared over varying azimuth. Another benefit of the paired instruments is to have a fall-back in very high flux regions; when EPT might saturate and have to filter out data, SATRAM can at least continue to record an integral flux. These are only a few potential complementarities that the two instruments have, and with the groundwork laid in this project, this and more can be put to use.

Of course, this project was undertaken with a view toward employing advanced radiation monitor data for physical investigations, alongside data from spectrometers such as EPT. Further work in this area has the potential to combine the benefits of each type of instrument, advancing our capabilities to understand space weather.

6 Bibliography and references

Anagnostopoulos, G., et al. *Radiation belt electron precipitation in the upper ionosphere at middle latitudes before strong earthquakes*, 2010. arXiv, https://arxiv.org/abs/1012.3588. Accessed 15 August 2021.

Borisov, Stanislav, et al. *Technical note 1B: Data analysis procedure for Proba-V/EPT spectra acquired after 15/09/2014*, Centre for Space Radiations, UCL, September 2019, EPT-DEXT-TN-011-CS.

Borisov, Stanislav, et al. *Technical note 1: The PROBA-V/EPT Data Analysis - Plan and S/W*, Centre for Space Radiations, UCL, July 2014, EPT-DE-TN-002-CS.

Cyamukungu, Mathias, et al. *The Energetic Particle Telescope (EPT) on board PROBA-V: description of a new science-class instrument for particle detection in space*, IEEE Transactions on Nuclear Science, vol. 61, no. 6, 2014, pp. 3667-3681.

European Space Agency *a*. *About Proba-V*, ESA, http://www.esa.int/Enabling_Support/Space_Engineering_Technology/Proba_Missions/About_Proba-V. Accessed 26 April 2021.

European Space Agency *b*. *Ending global plant tracking, Proba-V assigned new focus*, ESA, 20 May 2020, https://www.esa.int/Enabling_Support/Space_Engineering_Technology/Proba_Missions/Ending_global_plant_tracking_Proba-V_assigned_new_focus. Accessed 6 June 2021.

European Space Agency *c*. *PROBA-V*, Earth Online, https://earth.esa.int/eogateway/missions/proba-v. Accessed 6 June 2021.

Francois, Michael, et al. *The PROBA-V mission: the space segment*, International Journal of Remote Sensing, vol. 35, 2014, pp. 2548-2564, https://www.tandfonline.com/doi/abs/10.1080/01431161.2014.883098. Accessed 04 May 2021.

Granja, Carlos, et al. *a*. *Directional detection of charged particles and cosmic rays with the miniaturized radiation camera MiniPIX Timepix*, Nuclear Instruments and Methods in Physics Research, vol. 911, 2018, pp. 142-152.

Granja, Carlos, et al. *b*. *Resolving power of pixel detector Timepix for wide-range electron, proton and ion detection*, Nuclear Instruments and Methods in Physics Research, vol. 908, 2018, pp. 60-71.

Granja, Carlos, et al. *The SATRAM Timepix spacecraft payload in open space on board the Proba-V satellite for wide range radiation monitoring in LEO orbit*, Planetary and Space Science, vol. 125, 2016, pp. 114-129.

Gurman, Joseph B. *Solar Proton Events Affecting the Earth Environment*, NOAA Space Environment Services Center, National Oceanic and Atmospheric Administration, 2021, https://umbra.nascom.nasa.gov/SEP/. Accessed 15 August 2021.

Hadjas, Wojtek. *NGRM Next Generation Radiation Monitor new standard instrument for ESA*, 2016.

Holy, T., et al. *Pattern recognition of tracks induced by individual quanta of ionizing radiation in Medipix2 silicon detector*, Nuclear Instruments and Methods in Physics Research, vol. 591, 2008, pp. 287-290.

Kraft, Stefan, et al. *ESA's distributed space weather sensor system (D3S) utilizing hosted payloads for operational space weather monitoring*, Acta Astronautica, vol. 156, 2019, pp. 157-161.

Matzka, Jürgen, et al. *Geomagnetic Kp index. V. 1.0*, GFZ Data Services, https://doi.org/10.5880/Kp.0001. Accessed 21 July 2021.

Moldwin, Mark B. *An Introduction to Space Weather*, 1st ed., Cambridge, Cambridge University Press, 2008.

N2YO. *PROBA-V Satellite details*, N2YO.com, 2021, https://www.n2yo.com/satellite/?s=39159#. Accessed 04 May 2021.

NASA Marshall Space Flight Center. *Space Environments & Effects Program*, NASA, https://web.archive.org/web/20090320162405/http://see.msfc.nasa.gov/pf/pf.htm. Accessed 30 April 2021.

National Academy of Science. *Space Weather: A Research Perspective*, 1997. ww.nap.edu, The National Academies Press, https://doi.org/10.17226/12272. Accessed 21 July 2021.

National Observatory of Athens. *Radiation Belts and Trapped Particles*, MAARBLE Project, NOA Institute for Astronomy, Astrophysics, Space Applications and Remote Sensing, 2012, http://www.maarble.eu/outreach/index.php/basic-information. Accessed 21 July 2021.

National Oceanic and Atmospheric Administration. *Geomagnetic kp and ap Indices,* NCEI Solar-Terrestrial Physics, 2021, https://www.ngdc.noaa.gov/stp/GEOMAG/kp_ap.html. Accessed 04 May 2021.

Phillips, Tony. *Near Miss: The Solar Superstorm of July 2012*, NASA Science, NASA, 23 July 2014, https://science.nasa.gov/science-news/science-at-nasa/2014/23jul_superstorm/. Accessed 21 Jul 2021.

Pierrard, V., and G. L. Rosson. *The effects of the big storm events in the first half of 2015 on the radiation belts observed by EPT/PROBA-V*, Annales Geophysicae, vol. 34, no. 1, 2016, pp. 75-84.

Sullivan, J. D. *Geometrical factor and directional response of single and multi-element particle telescopes*, Nuclear Instruments and Methods, vol. 95, 1971, pp. 5-11.

Wilson, J. W., et al. *Overview of atmospheric ionizing radiation (AIR) Research: SST-present*, Advances in Space Research, vol. 32, no. 1, 2003, pp. 3-16.

7 Acknowledgements

This project was undertaken under the supervision of the promoters, Prof. Véronique Dehant and Prof. Denis Grodent. I would like to thank them first for their support and advice throughout this process of completing a master's thesis.

I would also like to thank my course co-ordinator Dr. Michaël De Becker, for his guidance from afar while I embarked on this project in a different country, and his generosity in answering my administrative questions.

I am grateful to the SATRAM team, particularly Dr. Carlos Granja, for providing their data for me to analyse, including several valuable updates during the project.

To my friends and my family, I express my deepest appreciation for keeping me sane and humouring me explaining all of this; especially to my brother Liam and partner Atlas.

Finally, my very best thanks is reserved for Sylvie Benck and Stanislav Borisov, without whom I couldn't have completed this work; not only because of their unparalleled technical knowledge about EPT and the related theory, nor their sound advice on writing a readable thesis, but especially the hours they spent with me reviewing my work, providing a wealth of good suggestions, and waiting patiently for my programs to run!